Formation of trapped vacuum bubbles during inflation, and consequences for PBH scenarios

Albert Escrivà a , Vicente Atal b and Jaume Garriga c

- ^aDivision of Particle and Astrophysical Science, Graduate School of Science, Nagoya University. Nagoya 464-8602, Japan
- ^bEstudio Ocho Casas, Calle Blanco 196, Papudo, Chile
- ^cDepartament de Física Quàntica i Astrofísica, i Institut de Ciències del Cosmos, Universitat de Barcelona. Martí i Franqués 1, 08028 Barcelona, Spain.

E-mail: escriva.manas.albert.y
0@a.mail.nagoya-u.ac.jp, vicente.atal@gmail.com, jaume.garriga@ub.edu

Abstract. A class of inflationary scenarios for primordial black hole (PBH) formation include a small barrier in the slope of the potential. There, the inflaton slows down, generating an enhancement of primordial perturbations. Moreover, the background solution overcomes the barrier at a very low speed, and large backward quantum fluctuations can prevent certain regions from overshooting the barrier. This leads to localized bubbles where the field remains "trapped" behind the barrier. In such models, therefore, we have two distinct channels for PBH production: the standard adiabatic density perturbation channel and the bubble channel. Here, we perform numerical simulations of bubble formation, addressing the issues of initial conditions, critical amplitude and bubble expansion. Further, we explore the scaling behaviour of the co-moving size of bubbles with the initial amplitude of the field fluctuation. We find that for small to moderate non-Gaussianity $f_{\rm NL} \lesssim 2.6$, the threshold for the formation of vacuum bubbles agrees with previous analytical estimates [1] to 5% accuracy or so. We also show that the mass distribution for the two channels is different, leading to a slightly broader range of PBH masses when both contributions are comparable. The bubble channel is subdominant for small $f_{\rm NL}$, and becomes dominant for $f_{\rm NL} \gtrsim 2.6$. We find that the mass of PBHs in the bubble channel is determined by an adiabatic overdensity surrounding the bubble at the end of inflation. Remarkably, the profile of this overdensity turns out to be of type-II. This represents a first clear example showing that overdensities of type-II can be dominant in comparison with the standard type-I. We also comment on exponential tails and on the fact that in models with local type non-Gaussianity (such as the one considered here), the occurrence of alternative channels can easily be inferred from unitarity considerations.

\mathbf{C}	ontents					
1	Introduction	1				
2	Set-up 2.1 Homogeneous inflationary dynamics 2.2 Perturbations 2.3 Local type non-Gaussianity	3 3 5 6				
	2.4 Probability distribution and the profile of high peaks2.5 Collapse of adiabatic fluctuations: threshold and PBH mass	8 10				
3	Bubble-formation					
4	Numerical strategy and details	14				
5	 Numerical results 5.1 Enhancement of cosmological fluctuations 5.2 Bubble dynamics formation and size 5.3 PBH production from the adiabatic and bubble channel 5.4 Mass function and spectrum of PBHs 	15 15 20 24 27				
6	Conclusion and discussion	31				
\mathbf{A}	Possible effect of mass accretion	33				
В	Numerical parameters data	33				

1 Introduction

Primordial black holes (PBH) forming during the radiation dominated era [2–6] (see [7] for a recent review), constitute a promising candidate for dark matter [8–14]. Although their dynamics does not involve any exotic physics beyond General Relativity, their formation requires certain assumptions about the initial conditions. These may be prepared during inflation, or at phase transitions in the early universe. PBH's have not been observed so far, but future gravitational wave observations may establish their existence [15–18].

A scenario which has received a great deal of attention in the literature is the collapse of large adiabatic perturbations generated during inflation. This requires a specific feature in the inflationary potential, enhancing the power spectrum by many orders of magnitude on a relatively narrow range of short distance scales, well below the CMB scales. The mass of the resulting more statistically relevant PBH's would be roughly of the order $M \sim (GH)^{-1}$, where H is the Hubble radius at the time when the short scale falls within the horizon during the radiation era [19].

A host of alternative mechanisms have been proposed, with very diverse statistical properties and PBH mass distributions (see [7] for a detailed list and a brief description). Of some relevance for the present work are spherical domain walls [20, 21], and vacuum bubbles [22–26] which may be produced by quantum tunneling during inflation. In such scenarios, tunneling is assumed to be a Poissonian process which can happen with nearly

constant probability per unit time and volume¹. Once formed, walls and vacuum bubbles are stretched to large sizes by the inflationary expansion, leading to a nearly scale invariant distribution of relics. After inflation, the interior of bubbles larger than a critical size will continue inflating in an ambient radiation-dominated Universe. This causes a particular form of gravitational collapse, where the bubble migrates from the parent universe and continues inflating in a baby universe². Parent and baby become causally disconnected soon after the co-moving scale of the bubble falls within the horizon and a trapped region forms. From then on, and from the point of view of the parent universe, one is left with a PBH whose mass is, again, of order $M \sim (GH)^{-1}$ a the time of formation. Domain walls above a certain critical size undergo a similar fate, due to their repulsive gravitational field.

Interestingly, vacuum bubbles may also arise naturally in models producing PBHs from large adiabatic fluctuations. In particular, this happens in single field models with a small barrier in the slope of the potential [27, 29–33]. The primary role of the barrier is to slow down the inflaton, thus producing an enhancement of curvature perturbations. On the other hand, large backward fluctuations can prevent localized domains from overshooting the barrier, resulting in vacuum bubbles where the field remains trapped behind the barrier [1, 27]. As a consequence, two different channels for PBH production coexist [1, 27]: the conventional one from large adiabatic fluctuations, and the bubble channel. The relative importance of both is determined by the sharpness of the barrier. This is in correspondence with the degree of non-Gaussianity of curvature perturbations at those scales, which can be characterized by the parameter $f_{\rm NL}$ in an expansion at low amplitudes. It was estimated in [1] that PBHs from vacuum bubbles would dominate for relatively sharp barriers, with $f_{\rm NL} \gtrsim 3.5$.

In a nutshell, this estimate follows from a non-perturbative relation $\zeta = \zeta(\zeta_G)$ between the curvature perturbation ζ and a Gaussian random field ζ_G , which was obtained analytically by using the δN formalism. The relation breaks down for $\zeta_G \gtrsim 1/f_{\rm NL}$, where ζ_G does not map into a finite or real value of ζ , Thus, while the distribution for ζ_G is normalized to one, the total probability for obtaining a finite value of ζ is less than one. Unitarity then suggests that values of $\zeta_G \gtrsim 1/f_{\rm NL}$ must correspond to an alternative channel. In the present case, it is natural to infer that this corresponds to large backward fluctuations producing vacuum bubbles. In order to confirm the accuracy of this argument, however, a numerical simulation is needed.

In what follows, we focus on models with a small barrier in the slope of the potential.

¹Such scenarios involve a multifield inflationary potential. For the case of domain walls, the simplest example is two field model with a standard slow roll potential in the inflaton direction ϕ , and with a discrete symmetry which acts in an orthogonal direction φ . In the φ direction the potential has the shape of a double well. In this way, the overall potential contains two parallel valleys. While the inflaton rolls down one of the valleys it has a finite probability per unit time and volume for transiting the neighboring valley by quantum tunneling accross the barrier. This results in the formation of a localized region of the new phase, which is separated from the old one by a domain wall. Under the assumption of near scale invariance, the rate of transition is nearly independent of time. This is only valid approximately, since tunneling rates are exponentially sensitive to parameters, and can vary significantly throughout the inflationary phase. If the double well in the φ direction is not degenerate, the discrete symmetry is broken, and we may expect the field in the new valley to get stuck in a different false vacuum. This leads to the formation of relic vacuum bubbles. Such scenarios are very different from the one we consider here, where we are considering single field dynamics, and barrier penetration is not involved.

²When the co-moving size of the vaccuum bubble falls within the horizon, its gravitational field carves a transient wormhole, similar to the Einstein-Rosen bridge of the extended Schwarzschild solution, and the bubble migrates to a baby universe. The bridge eventually pinches off at a black hole singularity. The black hole has two future event horizons, one facing the baby universe and one facing the ambient universe we inhabit [1, 21, 22, 27, 28].

A difference with the tunneling scenarios discussed in Refs. [21, 22, 28] is that, there, it is assumed that bubble nucleation happens at a nearly constant rate during inflation. Consequently the PBH mass function is rather broad. By contrast, in the present scenario, bubbles can only form near the time when the background solution is near the top of the barrier. This results in a sharply peaked co-moving size distribution. However, the width of this distribution can only be determined by numerical simulations, which have not been done so far.

With these issues in mind, the purpose of the present paper is a numerical study of the formation and evolution of trapped vacuum bubbles. Initial conditions will be derived from the spectrum of quantum fluctuations near the time when the background solution overshoots the barrier. We will then investigate the critical amplitude of the field fluctuation leading to bubble formation. We will also determine the scaling behaviour of the co-moving size of bubbles, as a function of the amplitude above the critical value. This will allow us to compare the numerical results with those inferred from analytical estimates. Finally, using the numerical results, we will estimate the abundance and mass function of PBH's from the two competing channels.

The plan of the paper is as follows: In Section 2, we describe the set-up and conventions. In Section 3, we describe the setup for bubble formation, including the use of consistent initial conditions. In Section 4 we discuss the numerical strategy and the details of the simulations we have implemented. In Section 5 we present our results. In particular, we discuss the numerical solution for the curvature fluctuations generated during inflation, the bubble dynamics, and the results for the PBH abundance and mass function. Section 6 is devoted to summary and conclusions, including perspectives for future work.

2 Set-up

In this section, we explain the basic setup and ingredients to study PBH formation from the collapse of adiabatic fluctuations. In particular, we consider the generation of the power spectrum of the curvature fluctuations, its statistical connection with the mean profile of the cosmological fluctuation, the role of non-Gaussianity, and finally the estimation of the threshold and PBH mass.

2.1 Homogeneous inflationary dynamics

Let us consider an inflationary scenario driven by a single scalar field, whose action (in Planck units, where $M_{\rm pl}=1/\sqrt{8\pi G}$ is the reduced Planck Mass) is given by

$$S = \int d^4x \sqrt{-g} \left[\frac{R}{2} - \frac{1}{2} \partial_\mu \phi \partial^\mu \phi - V(\phi) \right], \qquad (2.1)$$

where R is the Ricci scalar, and ϕ is the inflaton. For definiteness, we consider a Starobinsky-type potential [34] with a small barrier (or "bump") given by a Gaussian shape, which is modulated by parameters A (amplitude of the barrier), ϕ_0 (roughly location of the peak of the bump) and σ (the with of the bump):

$$V(\phi) = V_0^4 \left(1 - e^{-\sqrt{2/3}\phi} \right)^2 \left[1 + Ae^{-(\phi - \phi_0)^2/(2\sigma^2)} \right] . \tag{2.2}$$

We anticipate that the inflationary dynamics will be very sensitive to the specific values of the parameters, as was already noticed in [27]. A schematic picture of the potential is

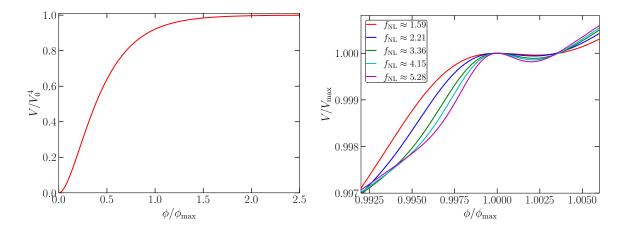


Figure 1. Left-panel: Inflationary potential $V(\phi)$ of Eq.(2.2) in terms of $\phi/\phi_{\rm max}$. Right-panel: Shape of the inflationary potential around the bump for different values of $f_{\rm NL}$. The value $\phi_{\rm max}$ indicates the location of the local maxima of the bump and $V_{\rm max} = V(\phi_{\rm max})$. The parameters chosen can be found in Table 1.

shown in Fig.1. The homogeneous dynamics of the inflaton field is obtained by solving the Klein-Gordon field equation on a FLRW (Friedmann-Lemaitre-Robertson-Walker) spacetime

$$ds^{2} = -dt^{2} + a^{2}(t)(dr^{2} + r^{2}d\Omega^{2}), \tag{2.3}$$

where t is the cosmic time, and a(t) is the scale factor. The Hubble rate is defined as $H = d \ln a/dt$, and for our purposes, it will be convenient to use the number of e-foldings N as our time variable. This is defined as $N = \int H dt$. The dynamics of the homogeneous background solution $\phi_{\text{bkg}}(N)$ is given by:

$$\ddot{\phi}_{\text{bkg}} + 3\dot{\phi}_{\text{bkg}} - \frac{1}{2}\dot{\phi}_{\text{bkg}}^3 + \frac{V_{\phi}(\phi_{\text{bkg}})}{V(\phi_{\text{bkg}})} \left(3 - \frac{\dot{\phi}_{\text{bkg}}^2}{2}\right) = 0.$$
 (2.4)

Here, and in what follows, a dot will indicate derivative with respect to N, that is $\dot{} \equiv d/dN$, V_{ϕ} is the derivative of the potential with respect to the field, and we have used $\dot{H} = -H\dot{\phi}_{\rm bkg}^2/2$ together with the Friedman equation,

$$H^{2} = \frac{V(\phi_{\text{bkg}})}{3 - \frac{\dot{\phi}_{\text{bkg}}^{2}}{2}}.$$
 (2.5)

The initial conditions for solving Eq.(2.4) are $\phi_{\rm bkg}(N_{\rm ini})$ where $N_{\rm ini}$ stands for the initial value of N, and $\dot{\phi}_{\rm bkg}(N_{\rm ini})$, which is obtained using the slow-roll approximation at $N_{\rm ini}$, $\dot{\phi}_{\rm bkg}(N_{\rm ini}) = -V_{\phi}(\phi_{\rm bkg}(N_{\rm ini}))/V(\phi_{\rm bkg}(N_{\rm ini}))$. It is useful to characterize the inflationary dynamics using the so-called Hubble slow-roll parameters defined as $\epsilon_{i+1} = d \ln \epsilon_i/dN$. The first two are given by $\epsilon_1 = \dot{\phi}_{\rm bkg}^2/2$ and $\epsilon_2 = \dot{\phi}_{\rm bkg} \ddot{\phi}_{\rm bkg}/\epsilon_1$. In the usual slow-roll (SR) phase, both ϵ_1 and $|\epsilon_2|$ are small, but a drastic reduction of the velocity of the inflaton $\dot{\phi}_{\rm bkg}$ (leading to large negative values of ϵ_2) can produce a significant enhancement of the primordial power spectrum responsible for the production of PBHs [35–38].

2.2 Perturbations

Scalar perturbations around the FLRW metric can be written in general as,

$$ds^{2} = a^{2}(\tau) \left[-(1+2A)d\tau^{2} + B_{,i}d\tau dx^{i} + \left[(1-2\Psi)\delta_{ij} + E_{,ij} \right] dx^{i} dx^{j} \right]$$
(2.6)

where $\tau = \int dt/a(t)$ is the conformal time, A is the lapse function, $B_{,i}$ is the shift, Ψ determines the curvature scalar of $\tau = const.$ surfaces, and E can be gauged away by spatial reparametrization. We are not including the tensor part since this will not play a role in our discussion. We may now define the gauge invariant combination [39, 40],

$$\zeta_G = -\left(\Psi + \frac{\delta\phi}{\dot{\phi}}\right),\tag{2.7}$$

which can be thought of as the spatial curvature of $\phi = const$. hypersurfaces. Since this is defined in linear theory, we call it the Gaussian curvature perturbation. Throughout this work, we will consider the constant mean curvature gauge (or "flat slicing"), where $\Psi = 0$, so that $\zeta_G \equiv -\delta\phi/\dot{\phi}$.

In Fourier space, the amplitude of Gaussian curvature fluctuations ζ_G is characterized by the power spectrum $P_{\zeta_G}(N,k)$, defined by

$$\langle \zeta_G(N, \mathbf{k}) \zeta_G(N, \mathbf{k}') \rangle = \frac{2\pi^2}{k^3} \mathcal{P}_{\zeta_G}(N, k) (2\pi)^3 \delta^{(3)}(\mathbf{k} + \mathbf{k}'), \tag{2.8}$$

where **k** denotes the wavenumber vector and k its modulus. The evolution of the modes $\zeta_G(N, \mathbf{k})$ is given by the Mukhanov-Sasaki (MS) equation [41, 42]:

$$\ddot{\zeta}_G + \left(1 - \frac{1}{2}\dot{\phi}_{\text{bkg}}^2 + 2\frac{\dot{z}}{z}\right)\dot{\zeta}_G + \left(\frac{k}{aH}\right)^2\zeta_G = 0,\tag{2.9}$$

where $z = a\dot{\phi}_{\rm bkg}$ with $\dot{z} = a(\dot{\phi}_{\rm bkg} + \ddot{\phi}_{\rm bkg})$, and H is given directly by Eq.(2.5) in terms of $\phi_{\rm bkg}$.

The positive frequency modes ζ_G can be obtained numerically by solving Eq.(2.9) and using the inflationary homogeneous solution for $\phi_{\text{bkg}}(N)$ obtained from Eq.(2.4). We use the Bunch-Davies initial conditions [43] in Eq.(2.9), at a time characterized by N_i when the modes are well inside the horizon $(k \gg aH)$,

$$Re[\zeta_G] = \frac{1}{\sqrt{2k}} \frac{1}{z(N_i)}, \qquad Im[\zeta_G] = 0,$$

$$Re[\dot{\zeta}_G] = -\frac{1}{2k} \frac{1}{z(N_i)} \left(\frac{\ddot{\phi}_{bkg}(N_i)}{\dot{\phi}_{bkg}(N_i)} + 1 \right), \quad Im[\dot{\zeta}_G] = -\sqrt{\frac{k}{2}} \frac{1}{a(N_i)H(N_i)z(N_i)}.$$
(2.10)

From ζ_G we can compute the dimensionless power spectrum of the curvature fluctuation, which is given by

$$\mathcal{P}_{\zeta_G}(N,k) = \frac{k^3}{2\pi^2} |\zeta_G(N,k)|^2.$$
 (2.11)

The power spectrum becomes frozen at sufficiently large scales, much larger than the Hubble radius $k \ll aH$.

At the linear order in the Hubble parameters and assuming the slow-roll approximation, curvature fluctuations are frozen soon after horizon crossing. In this case, their power spectrum at super horizon scales is given by [44],

$$\mathcal{P}_{SR}(k) = \left. \frac{H^2}{8\pi^2 \epsilon_1} \right|_{k=aH}.$$
(2.12)

In our case, this expression is valid on CMB scales. At the much shorter PBH scales, departures from slow-roll will be important, and curvature perturbations may have a significant time dependence after horizon crossing. For that reason, their amplitude at the end of inflation will be computed numerically as outlined above³. The parameters of the inflationary potential in Eq.(2.2) are chosen so that they fulfill the CMB constraints, and result in a sufficient duration of inflation. In particular: i) the power spectrum at the CMB scales at a reference scale $k_{\text{pivot}} = a(N_{\text{pivot}})H(N_{\text{pivot}}) = 0.05\text{Mpc}^{-1}$ should be $\mathcal{P}_{\zeta_G}(k_{\text{pivot}}) = (2.2 \pm 0.1) \cdot 10^{-9}$ with a spectral index $0.9565 \le n_{\text{s}} \le 0.9733$ and tensor ratio $r \le 0.06$ at the 95% confident level [46, 47] and, ii) the number of e-folds between the end of inflation and the pivot scale must be $44.02 \le N_{\text{end}} - N_{\text{pivot}} \le 54.88$ [48–50].

2.3 Local type non-Gaussianity

The intrinsic non-Gaussianity $\delta\phi$ which is present before entering the attractor regime in the flat slicing can be estimated to be of order ϵ [51], which is less than 10^{-2} in our model. This means that $\zeta_G \equiv -\delta\phi/\dot{\phi}$ is also nearly Gaussian around the time of horizon crossing. On the other hand, the relation between ζ_G and the actual curvature perturbation ζ , which determines the magnitude and fate of overdensities in the radiation dominated era, is highly non-linear in the range of interest. Therefore ζ is not a Gaussian random field.

Fortunately, a local relation $\zeta = \zeta(\zeta_G)$ can be found which applies to the present situation [27], by using the δN formalism. For the sake of clarity, let us briefly review the derivation. Since the height of the barrier is tiny compared to the overall potential, we can safely assume that H is approximately constant. In the vicinity of the local maximum $\phi = \phi_{\text{max}} \approx \phi_0$, the potential can be approximated by a quadratic term, and the inflaton behaves as a free field with constant negative mass squared $m^2 \equiv V_{\phi\phi}(\phi_{\text{max}}) < 0$ in de Sitter. The background solution can then be written as

$$\phi_{\text{bkg}}(N) - \phi_{\text{max}} = \tilde{A} \left[e^{-\lambda_{-}\Delta N} - e^{-\lambda_{+}\Delta N} \right],$$
 (2.13)

where we have introduced the notation

$$\lambda_{\pm} = \frac{3}{2} \pm \alpha, \quad \alpha \equiv \sqrt{9/4 - m^2/H^2} > 3/2,$$
(2.14)

and $\Delta N = N - N_{\text{max}}$. The integration constant \tilde{A} is related to the speed at the top of the barrier $\tilde{A} = (2\alpha)^{-1}\dot{\phi}_{\text{max}}$. Consider now some N_{\star} such that

$$\exp[2\alpha(N_{\star} - N_{\text{max}})] \gg 1. \tag{2.15}$$

Since $2\alpha > 3$, it is clear that this will be satisfied very soon after the maximum, for

$$N_{\star} \geq N_{\text{max}} + \mathcal{O}(1).$$

³For an analytical approach, see [45].

At later times, the hyperbolic function behaves like a growing exponential, and we have

$$\phi_{\text{bkg}}(N) - \phi_{\text{max}} \approx \tilde{A} e^{-\lambda_{-}\Delta N}, \quad (N \ge N_{\star}).$$
 (2.16)

In the long wavelength limit, when $k^2/a^2 \ll |m^2| + H^2$, a generic perturbation can be written as $\delta\phi = \tilde{B}e^{-\lambda_+\Delta N} + \tilde{C}e^{-\lambda_-\Delta N}$. Near the time of horizon crossing, one expects that growing and decaying components may have comparable magnitude. If this happens before reaching the top, then one expects that by $N \approx N_{\rm max}$ the growing component will be at least comparable to the decaying one. In this case, we have $\tilde{B} \lesssim \tilde{C}$, and therefore

$$\delta \phi \approx \tilde{C} e^{-\lambda_- \Delta N} \propto \dot{\phi}_{\rm bkg}. \quad (N \ge N_\star)$$
 (2.17)

Therefore, for $N > N_{\star}$ we have $\delta \dot{\phi} = -\lambda \delta \phi \propto \dot{\phi}$. Since the momentum perturbation is determined by the field perturbation, we call this the attractor behaviour.

From then on, the Gaussian curvature perturbation stays constant, and is given by

$$\zeta_G(N > N_{\star}) = -\frac{\delta\phi}{\dot{\phi}_{\text{bkg}}} \bigg|_{N_{\star}}.$$
(2.18)

Here, $\delta \phi$ is evaluated on a flat slice with $N = N_{\star}$. Alternatively, we may write

$$\phi_{\text{bkg}}(N) + \delta\phi(N, \mathbf{x}) = \phi_{\text{bkg}}(N + \delta N(\mathbf{x})), \tag{2.19}$$

so that the perturbed field $\phi_{\text{bkg}} + \delta \phi$ is constant on the slice with $N + \delta N = const.$ As usual, δN has the meaning of the decrease in the number of e-foldings from a flat slice until the end of inflation, due to the field perturbation.

It follows from (2.16) and (2.19) that for $N > N_{\star}$ we have $\lambda_{-}\delta\phi/\dot{\phi}_{\rm bkg} = 1 - e^{-\lambda_{-}\delta N}$. The non-linear curvature perturbation $\zeta = -\delta N$ can then be expressed as [1, 27] ⁴

$$\zeta = -\mu_{\star} \ln \left(1 - \frac{\zeta_G}{\mu_{\star}} \right), \qquad (N > N_{\star}) \tag{2.20}$$

where we have introduced

$$\mu_{\star} \equiv -\lambda_{-} = \sqrt{\frac{9}{4} - 3\frac{V_{\phi\phi}(\phi_{\text{max}})}{V(\phi_{\text{max}})}} - \frac{3}{2} > 0.$$
 (2.21)

In the last equality we have substituted m^2 and H in terms of the inflationary potential and its derivatives at the local maximum⁵.

It is customary to characterize local non-Gaussianity by the coefficient $f_{\rm NL}$ of the quadratic term in a perturbative expansion [53],

$$\zeta \approx \zeta_G + \frac{3}{5} f_{\text{NL}} \zeta_G^2 + \dots \tag{2.22}$$

⁴Similar expressions were recently discussed in [52], where more general potentials are considered. Applied to the present case, the formalism of [52] can be shown to reproduce Eq.(2.20). Note that we are not neglecting $\delta\dot{\phi}$ on the initial flat slice. Also, we are not requiring that the solution be in the attractor regime already at the maximum of the potential. Rather, as pointed out after Eq.(2.15), we expect the attractor to hold shortly after.

 $^{^5}$ Eq.(2.20) will not necessarily hold for modes that cross the horizon much later than $N_{\rm max}$. Although an attractor will eventually be reached, and ζ_G will freeze, this may happen in a regime where the quadratic approximation to the potential is no longer valid. Then, due to the more complicated form of the background solution $\phi_{\rm bkg}(N)$, the relation between ζ_G and ζ may in general be different.

From (2.20) with $\zeta_G \ll \mu_{\star}$ we can identify,

$$f_{\rm NL} = \frac{5}{6\mu_{\star}}.\tag{2.23}$$

This agrees with a perturbative determination of non-Gaussianity, which can be obtained diagramatically [36, 54]. Here, however, we are interested in the case where both $f_{\rm NL}$ and ζ_G are $\mathcal{O}(1)$, and a truncation of the series is not useful. Hence, in what follows we will rely on the full non-perturbative expression (2.20), using $f_{\rm NL}$ only as a proxy for different shapes of the barrier (see the right panel of Fig. 1). A sharper bump around $\phi_{\rm max}$ corresponds to higher values of $f_{\rm NL}$, and vice versa.

2.4 Probability distribution and the profile of high peaks

The relation (2.20) has a major impact in the probability distribution of adiabatic perturbations, affecting both the amplitudes and profiles of high peaks. These are key ingredients in assessing the resulting distribution of PBH, which require some discussion.

Here, and in what follows, we take the point of view that ζ_G is the fundamental random variable, with a normalized Gaussian distribution, $P_G[\zeta_G]$. One can of course derive from it a PDF for ζ ,

$$P[\zeta] = P_G[\zeta_G(\zeta)] \frac{d\zeta_G}{d\zeta}.$$
 (2.24)

From (2.20), we have $\zeta_G = \mu(1 - e^{-\zeta/\mu_*})$. In the limit $\zeta \to \infty$, we have $\zeta_G \to \mu_*$, and the first factor in the right hand side of (2.24) remains finite. The Jacobian, on the other hand, is given by $(d\zeta_G/d\zeta) = e^{-\zeta/\mu_*}$, leading to an "exponential tail" in the distribution

$$P[\zeta] \propto e^{-\zeta/\mu_{\star}}. \quad (\zeta \to \infty)$$
 (2.25)

This is in contrast with the stronger Gaussian suppression of P_G at large ζ_G , a fact has been noticed e.g. in [52] and references therein. This behaviour, however, stems from the vicinity of a point $\zeta_G = \mu_{\star}$ where the Jacobian is singular.

In our view, therefore, what is really interesting about the tail is not so much the limit $\zeta \to \infty$, but what lies beyond that limit, in the regime $\zeta_G > \mu_{\star}$. In other words, although $P_G[\zeta_G]$ is normalized, $P[\zeta]$ is not because the full range of ζ corresponds to a restricted range of ζ_G :

$$\int P[\zeta] D\zeta = \int_{\zeta_G < \mu_{\star}} P_G[\zeta_G] D\zeta_G < 1.$$
(2.26)

The broader lesson is that a singularity in a local non-Gaussianity relation $\zeta(\zeta_G)$ indicates the presence of alternative channels, which restore unitarity⁶. This will be our focus here.

PBH originate from rare fluctuations of the Gaussian random field ζ_G , with amplitude μ much larger than the standard deviation, $\mu \gg \sigma_0$. Here, we use the notation

$$\sigma_n^2(N) = \int k^{2n} \mathcal{P}_{\zeta_G}(N, k) d\ln k. \tag{2.27}$$

Although perturbations are frozen at sufficiently large scales, for the sake of future reference here we keep the possibility that some of the modes may still be evolving. The N dependence

⁶Related interesting examples of local non-gaussianity leading to two different channels for PBH formation are studied in [55, 56].

of \mathcal{P}_{ζ_G} and derived quantities will not be displayed explicitly in what follows, but it should be implicitly understood. Also, in practice, we cut off the momentum integrals at the UV. This regulator is equivalent to a top-hat window function, which eliminates short distance contributions not relevant to the problem.

Rare fluctuations with amplitude $\mu = \nu \sigma_0$, where $\nu \gg 1$ tend to be spherically symmetric. The mean profile for given ν takes the form [57]

$$\langle \zeta_G(r) \mid \nu \rangle = \mu \Psi_{\zeta_G}(r)$$
 (2.28)

where we have introduced the normalized two-point correlation function:

$$\Psi_{\zeta_G}(r) = \frac{1}{\sigma_0^2} \langle \zeta_G(r)\zeta_G(r=0) \rangle = \frac{1}{\sigma_0^2} \int \mathcal{P}_{\zeta_G}(k)\operatorname{sinc}(kr)d\ln k.$$
 (2.29)

This function has a maximum at r = 0, with $\Psi_{\zeta_G}(r = 0) = 1$, and typically decays to zero for large r. The deviations from the mean profile are characterized by the variance⁷

$$<(\Delta\zeta_G)^2> = \sigma_0^2[1-\Psi_{\zeta_G}^2(r)].$$
 (2.30)

Hence, the profile can be approximated as

$$\zeta_G(r) = \mu \Psi_{\zeta_G}(r) \pm \Delta \zeta_G. \tag{2.31}$$

The correction $\Delta \zeta_G$ of order σ_0 need not be spherically symmetric, and has the variance given by (2.30). For $\mu \gg \sigma_0$ this term is small by comparison, and so we are led to the conclusion that high peaks are nearly spherically symmetric. Furthermore, such variance goes to zero as we approach r=0, where $\Psi_{\zeta_G}=1$. Hence, the non-sphericity is only appreciable far away from the center. For given μ , 68% of all configurations of ζ_G are contained within the bundle (2.31) of width $\Delta \zeta_G$ around the mean value. Here, we shall simply consider the mean configuration as a fair representative for each bundle⁸.

The amplitude μ follows the Gaussian distribution,

$$P(\mu) = \frac{1}{\sqrt{2\pi\sigma_0^2}} e^{-\frac{\mu^2}{2\sigma_0^2}},\tag{2.32}$$

and in the limit $\nu \gg 1$, the number density of peaks $\mathcal{N}_{pk}(\nu)$ is given by [57]

$$\mathcal{N}_{\rm pk}(\nu)d\nu = \left(\frac{\sigma_1}{\sqrt{3}\sigma_0}\right)^3 (\nu^3 - 3\nu)e^{-\frac{1}{2}\nu^2}d\nu, \tag{2.33}$$

⁷Here we are not requiring that the value of ν corresponds to a peak. Expressions with this restriction are more cumbersome, and can also be found in [57]. The difference can be appreciable for low to moderate ν . However, the distinction seems hardly relevant for $\nu \sim 10$, which is the case of interest for PBH formation. Places where $\nu \sim 10$ are so rare, that for practical purposes they have to be either at a maximum, or very close to one.

⁸In Refs.[1, 27] the images $\{\zeta[\zeta_G]\}$ of such bundles under the mapping (2.20) were considered. For the case $\nu=5$, it was found that such images have some dispersion $\Delta\mu$ in the critical value of the amplitude $\mu=\mu_c$ leading to PBH formation. The differences with the mean configuration were of order $\Delta\mu/\mu\sim10\%$ at low $f_{\rm NL}\lesssim1$, but quickly dropped to less than 2.5% or so for $f_{\rm NL}\gtrsim2$. Here we are considering $\nu\sim10$ instead, and so we expect the relative dispersion to be smaller. A fair sampling of the bundle is computationally expensive and oustide the scope of the present work. Hence, we leave this as a subject for further research.

where the σ_n are computed following Eq.(2.27). We will estimate PBH abundances and the mass function following this statistical description accounting for peaks in the curvature fluctuation ζ_G .

As argued in [1, 27], perturbations for which $\mu \geq \mu_{\star}$ correspond to portions of the universe that fall back in the false minimum of the potential behind the barrier, leading to trapped vacuum bubbles. These do not admit a description in terms of ζ , simply because inflation does not end inside the bubbles and δN is formally divergent. On the other hand, perturbations with $\mu < \mu_{\star}$ might form PBHs from the collapse of the adiabatic fluctuations. Let us now consider the two channels for PBH production in more detail.

2.5 Collapse of adiabatic fluctuations: threshold and PBH mass

From now on, μ_a denotes the amplitude of the adiabatic perturbation. The associated profile $\Psi_a \equiv \Psi_{\zeta_G}$ and variance $\sigma_a \equiv \sigma_0(N \gg N_\star)$ are calculated from the power spectrum once all relevant wavelengths are frozen in, near the end of inflation. Sufficiently large super-horizon fluctuations ζ above the critical threshold value $\mu_a > \mu_{a,c}$ will collapse forming black holes after horizon reentry in the radiation dominated era. These fluctuations will initially be at super-horizon scales, fulfilling that $\epsilon \equiv R_H/R_m \ll 1$, where ϵ is a dimensionless parameter relating two scales: the Hubble horizon R_H and the length-scale of the fluctuations R_m . In the limit $\epsilon \to 0$ and under the assumption of spherical symmetry⁹, it was shown in [58] that the spacetime metric locally corresponds to

$$ds^{2} = -dt^{2} + a^{2}(t)e^{2\zeta(r)}\left(dr^{2} + r^{2}d\Omega^{2}\right). \tag{2.34}$$

Notice that $\zeta(r)$ is time independent at super-horizon scales since $\partial \zeta/\partial t \sim \mathcal{O}(\epsilon^2)$ [58–61].

A useful quantity to measure the strength of a spherically symmetric fluctuation is the compaction function (introduced in [58]), that quantifies the mass excess enclosed in the area radius R(r,t) relative to the FLRW background $M_{\rm bkg} = 4\pi \rho_{\rm bkg} R^3/3$,

$$C(r,t) = 2\frac{M(r,t) - M_{\text{bkg}}(r,t)}{R}.$$
(2.35)

At super-horizon scales, the compaction function turns out to be time-independent and is related to the curvature fluctuation ζ^{10} as [62]

$$C(r) = \frac{2}{3} \left[1 - (1 + r\zeta'(r))^2 \right] + O(\epsilon^2), \tag{2.36}$$

where the factor 2/3 accounts for a radiation-dominated Universe. In [63], it was shown that the averaged critical compaction function $\bar{\mathcal{C}}_c$ integrated up to its peak value r_m is a good estimator to characterize the threshold for PBH formation giving a universal critical value

$$\bar{\mathcal{C}}_c = 2/5. \tag{2.37}$$

 $^{^9}$ A discussed above, in the limit $\nu \gg 1$, fluctuations can be considered approximately spherically symmetric. This consideration extends to the presence of NGs if the peaks are sufficiently large. See previous footnote.

¹⁰Adiabatic fluctuations are characterized by a single variable. Historically, the density contrast $\delta \equiv (\rho - \rho_b)/\rho_b$ has often been used in discussions of critical collapse. However it is more convenient to use the curvature perturbation ζ instead. In the limit of slow-roll parameters the latter variable is Gaussian, while δ is not. Here ζ will not be Gaussian, but it is a local function of a Gaussian variable ζ_G . From ζ one can always obtain δ , but this operation is unnecessary. The numerical code is written directly in terms of ζ .

This estimator was found to be independent of the shape of the curvature fluctuation within a $\sim 2\%$ deviation, for a wide class of cosmological relevant curvature profiles (see [64] for a generalization to other perfect fluid equations of state, different from radiation)¹¹. More explicitly, \bar{C}_c is defined as

$$\bar{C}_c = \frac{3}{r_m^3(\mu_{a,c})e^{3\zeta(r_m(\mu_{a,c}))}} \int_0^{r_m(\mu_{a,c})} C_c(r)(1+r\zeta')e^{3\zeta(r)}r^2dr.$$
 (2.38)

For a Gaussian random field, the position of the peak of the compaction function r_m (obtained solving $\zeta'(r_m) + r_m \zeta''(r_m) = 0$ from Eq.(2.36)), does not depend on the amplitude of the fluctuation. However, in the presence of NGs, r_m does depend on the amplitude μ_a , since the shape of the non-gaussian peak depends non-linearly on that parameter. Therefore we have included a dependence $r_m(\mu_{a,c})$ in Eq.(2.38). Notice that two types of fluctuations can be differentiated. Fluctuations of type-I (the "standard" ones) satisfy that the areal radius $R = a r e^{\zeta}$ is monotonically increasing in r. Instead, fluctuations of type-II [65] fulfil that there is a point r_{II} such that $R'(r_{II}) = 0$, which makes R a non monotonic increasing function R' < 0. This condition translates to $1 + r_{II}\zeta'(r_{II}) = 0$ which implies that the peak value of the compaction function is 2/3, its maximum possible value in a radiation-dominated Universe. Fluctuations of type-II are usually neglected in the literature and considered unimportant for the estimation of PBH abundances since they are highly over-threshold and, therefore, statistically suppressed. The behaviour and dynamics of fluctuations of type-I have been studied in detail thanks to numerical simulations (see [66] for a review), but this is not the case for type-II (except the analytical exploration done in [65]), for which numerical studies are needed. In this work we use the remarkable result of $\bar{\mathcal{C}}_c = 2/5$ to obtain the threshold $\mu_{a,c}$ without the need to perform systematic numerical simulations¹² of the gravitational collapse of the adiabatic fluctuations from the adiabatic channel. This analytical approach has been used successfully already in the context of non-gaussianities in [1, 68, 69]. The details about the numerical approach are given in section 4.

The PBH mass from the collapse of adiabatic fluctuations follows a critical collapse regime for fluctuations amplitudes μ_a close to the critical value $\mu_a \to \mu_{a,c}$ [70–72]. In particular, taking into account the relation of horizon crossing $r_m e^{\zeta(r_m)} = k^{-1}$ (the fluctuation reenters the cosmological horizon at the time t_H , for which $a(t_H)H(t_H)r_m e^{\zeta(r_m)} = 1$), the PBH mass is given by [68]

$$M_{\text{PBH}}(\mu_a) = \mathcal{K}_a(\mu_{a,c}) M_k(k) x_m^2(\mu_a) e^{2\zeta(r_m(\mu_a))} (\mu_a - \mu_{a,c})^{\gamma_a}, \qquad (2.39)$$

where $x_m(\mu_a) = r_m(\mu_a)k$. The term $M_k(k)$ is the mass of the cosmological horizon when the single mode k (given in units of Mpc⁻¹) reenters it [68, 73]

$$M_k(k) \approx 10^{20} \left(\frac{g_{\star}}{106.75}\right)^{-1/6} \left(\frac{k}{1.56 \cdot 10^{13} \text{Mpc}}\right)^{-2} 5.027 \cdot 10^{-34} M_{\odot},$$
 (2.40)

¹¹Such a result allows to build an analytical formula for the threshold values in terms of a dimensionless parameter that characterizes the shape around the compaction function peak [63]. See [63] for details.

¹²We have indeed verified using simulations of the gravitational collapse of the adiabatic fluctuations using the publicly available code of [67] that for the profiles ζ under consideration the thresholds are within $\sim 1\%$ deviation compared with the ones obtained following the analytical approach. For the smaller case of $f_{\rm NL}$ that we consider, we have $\sim 1\%$ deviation, and it becomes smaller when increasing the value of $f_{\rm NL}$ since $\mu_a \to \mu_{\star}$. Indeed, numerical simulations for $f_{NL} > 3.5$ has been shown to be numerically challenging. Therefore in this work we use the analytic estimate based on the averaged critical compaction function to obtain $\mu_{a,c}$.

where γ_a is a critical universal exponent (independent of the shape of the curvature fluctuation) found to be $\gamma_a \approx 0.356$ for radiation [70, 72, 74]. We also take $g_\star \sim 106.75$ (the effective number of degrees of freedom for the energy density of the cosmic fluid at the at the time the scale k reenters the horizon) uniformly in our PBH mass range as in [68]. For simplicity, we are going to consider a constant value for $\mathcal{K}_a(\mu_{a,c}) = \mathcal{K}_a = 6^{13}$, which corresponds to the value we have found using numerical simulations for $f_{\rm NL} \approx 1$ (the value of \mathcal{K} depends on the shape of the fluctuation and $f_{\rm NL}$ modulates it). For other cases, we expect a small deviation within a factor [0.5, 3] (see Fig.9 in [75]). In 5.4, we give details about the procedure followed to estimate the corresponding mass function to PBH abundances.

3 Bubble-formation

Let's move now to study the channel of PBH production from vacuum bubbles, which needs a detailed discussion. For sufficiently large backward quantum fluctuations, the inflaton field cannot overshoot the barrier and exit inflation, forming trapped vacuum bubbles. This is schematically represented in Fig.2. In Ref. [1] $\mu_a = \mu_{\star}$ was considered to be the threshold for vacuum bubble formation, so that for $\mu_a > \mu_{\star}$ a localized region becomes trapped in the false vacuum. Here, we intend to simulate this process in order to check the validity of this estimation. Therefore, we should define a new amplitude variable μ_b to characterize the fluctuations leading to bubble formation, different from μ_{\star} . The dynamics of the inflaton field under spherical symmetry with a radial dependence $\phi(N, \tilde{r})$ is approximately ¹⁴ given by

$$\ddot{\phi} + \dot{\phi} \left(3 - \frac{1}{2} \dot{\phi}_{\text{bkg}}^2 \right) - \left(\frac{a_I H_I}{a(N)H(N)} \right)^2 \Delta \phi + \frac{1}{H^2} \frac{V_{\phi}(\phi)}{V(\phi)} = 0, \tag{3.1}$$

where ϕ_{bkg} corresponds to the background dynamics solution obtained solving Eq.(2.4) and Δ is the Laplacian operator in spherical coordinates. We have included a rescaling on the radial coordinate r in terms of the comoving Hubble scale $a_I H_I$ as $\tilde{r} = r \cdot (a_I H_I)$, where the sub-index I refers to the time when the initial conditions are set. The consideration of what initial conditions should be introduced is essential, since the dynamics will be strongly dependent on that.

As shown in Fig.2, we consider that at a specific time N_{\star} after the background field has overshoot the potential barrier, the accumulated inflaton fluctuation at a specific point corresponds to a backward jump of magnitude $\delta \phi$. At this time we have

$$\phi(N_{\star}, \tilde{r}) = \phi_{\text{bkg}}(N_{\star}) + \delta\phi(N_{\star}, \tilde{r}), \tag{3.2}$$

$$\dot{\phi}(N_{\star}, \tilde{r}) = \dot{\phi}_{\text{bkg}}(N_{\star}) + \delta \dot{\phi}(N_{\star}, \tilde{r}). \tag{3.3}$$

The field perturbation $\delta \phi$ is calculated from the power spectrum of the field ϕ at the time N_{\star} , which we denote as $\mathcal{P}_{\delta \phi}(N_{\star}, k)$. This is computed numerically by solving the MS equation,

¹³This simplification is commonly done in the literature, since the constant \mathcal{K}_a appears just as a linear factor in the PBH mass, and it's precise value $\mathcal{O}(1)$ is does not significantly change the PBH abundance and the mass function.

¹⁴The approximation is that the Hubble rate is determined by the background solution, but the gravitational field of the bubble is ignored. This is a very good approximation during bubble formation, since the height of the barrier is insignificant compared with the overall size of the potential. Nonetheless, it should be kept in mind that once a bubble forms, the field in its interior is stuck in the false vacuum. Hence, near the end of inflation and during the radiation era, the inside will eventually expand at a faster rate than the environment.

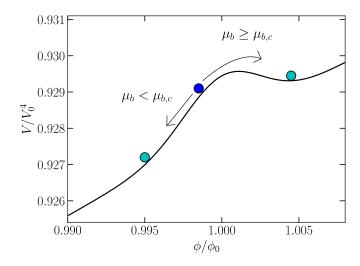


Figure 2. Schematic picture of a bubble formation. For fluctuations above the threshold $\mu_b > \mu_{b,c}$ a localized region will become trapped producing a vacuum bubble. In the opposite case, for sub-critical fluctuations $\mu_b < \mu_{b,c}$ the inflaton overshoots the barrier.

and evaluating the curvature modes right at N_{\star}

$$\mathcal{P}_{\delta\phi}(N_{\star}, k) = \frac{k^3}{2\pi^2} \dot{\phi}_{\text{bkg}}^2(N_{\star}) | \zeta_G(N_{\star}, k) |^2.$$
 (3.4)

By analogy with the case of adiabatic curvature perturbations, we can compute the two-point correlation function $\Psi_b(\tilde{r})$ associated with $\delta\phi$ as

$$\Psi_b(N_{\star}, \tilde{r}) = \frac{1}{\sigma_b^2} \int_{k_{\star}}^{k_f} \mathcal{P}_{\delta\phi}(N_{\star}, k) \operatorname{sinc}(k\tilde{r}) d\ln k, \tag{3.5}$$

where σ_b is the variance of the power spectrum $\mathcal{P}_{\delta\phi}$, and we can define $\nu_b = \mu_b/\sigma_b$. Then the initial value of the field fluctuation is given by

$$\delta\phi(N_{\star},\tilde{r}) = \mu_b \Psi_b(N_{\star},\tilde{r}). \tag{3.6}$$

The limits of integration k_f and k_i deserve some discussion. These are chosen so that we include all modes that have been enhanced by the dynamics while the scalar field overshoots the barrier, regardless of whether they are frozen in or not at the time N_{\star} . On the other hand, we exclude UV contributions whose amplitude is the same as in flat space. More explicitly, we will consider that a mode has been enhanced at a given scale when the power spectrum is much larger than the one for a scalar field in a Minkowski vacuum, at the same physical scale

$$\mathcal{P}_{\delta\phi}(N_{\star},k) \gg \frac{k^2}{a^2(2\pi)^2}.\tag{3.7}$$

For a massless field, this holds on superhorizon scales, $k \ll aH$. In our case, $\mathcal{P}_{\delta\phi}(N,k)$ may start growing before horizon crossing, since the effective mass squared is negative, $m^2 = V_{\phi\phi} < 0$, near the top of the barrier. This triggers exponential growth of modes with $k^2 \ll a^2 |m^2|$. By the time N_{\star} some modes can be excited with a large variance even if they are still subhorizon. In practice, we will use the condition (3.7) in order to determine the limits of integration in Eq.(3.5).

In quantum theory, it is not possible to simultaneously specify the field $\delta\phi$ and its conjugate momentum $\delta\pi = a^3H\delta\dot{\phi}$, due to the uncertainty principle. However, here we are dealing with modes whose variance is strongly enhanced relative to the zero point fluctuation, as in Eq.(3.7). Also, the anticommutator of field and momentum conjugate is much larger than their commutator¹⁵. Hence, it seems appropriate to treat such excitations as a classical ensemble. As discussed in Subsection 2.3, there is a specific attractor regime for $N \approx N_{\star}$ where $\dot{\phi}_{\rm bkg} \approx -\lambda_{-}(\phi_{\rm bkg} - \phi_{\rm max})$, which also holds for the perturbations [27]

$$\delta \dot{\phi} \approx -\lambda_{-} \delta \phi, \tag{3.8}$$

as discussed after Eq.(2.17). The attractor behavior will not be exact, and we have to numerically monitor to what extent it is satisfied. To optimize our strategy, we define N_{\star} as the time that minimes the departure from the attractor regime, i.e.

$$\Delta_{\rm att}(N_{\star}) = \frac{\dot{\phi}_{\rm bkg}(N_{\star}) + \lambda_{-}(\phi_{\rm bkg}(N_{\star}) - \phi_{\rm max})}{\dot{\phi}_{\rm bkg}(N_{\star})}.$$
 (3.9)

As we shall see, for small $f_{\rm NL}$ the attractor holds to good approximation for a brief interval of e-folds. However, it becomes less well defined for large non-Gaussianity, $f_{\rm NL} \gtrsim 3.5$ (see caption in Fig.5). This will make our choice of initial conditions less reliable at high values of $f_{\rm NL}$.

4 Numerical strategy and details

To perform the numerical simulations we have developed a numerical code based on *Python* [76] that allows us to solve in independent blocks the different numerical procedures and simulations that are needed. We take the profit of some implemented procedures to solve differential equations using *Numpy* and *Scipy* libraries [77, 78]. By order of application, we give general details of the implementation as follows:

- Block I (homogeneous solution): For each set of parameters of Eq.(2.2) (see Tables 1 and 2), we first solve the background dynamics of the field Eq.(2.4) numerically to obtain $\phi_{\text{bkg}}(N)$ and $\dot{\phi}_{\text{bkg}}(N)$. The background solution is then used to solve the MS equation numerically using Eq.(2.10) as the initial conditions for modes well inside the cosmological horizon $k \sim 10^3 a(N_{\text{crossing}})H(N_{\text{crosing}})$. From there we obtain the power spectrum \mathcal{P}_{ζ_G} (the modes ζ_G are evaluated at super-horizon scales, when the modes are frozen with $k \sim 10^{-4} a(N_{\text{crossing}})H(N_{\text{crosing}})$) and $\mathcal{P}_{\delta\phi}$ (we evaluate ζ_G at N_{\star}). Using them, we compute the corresponding two point-correlation functions $\Psi_a(\tilde{r})$ and $\Psi_b(N_{\star}, \tilde{r})$ making numerically an anti-Fourier transformation. We rescale the radial coordinate as the comoving Hubble horizon at N_{\star} given by $1/(a(N_{\star})H(N_{\star}))$, where N_{\star} is found numerically as the value that minimizes Eq.(3.9).
- Block II (adiabatic channel): Using $\Psi_a(\tilde{r})$ we build the mean Gaussian curvature shape ζ_G and the corresponding non-Gaussian curvature ζ with amplitude μ_a and corresponding parameter $f_{\rm NL}$. We perform a bisection on μ_a to find the critical value $\mu_{a,c}$ such that the averaged critical compaction function is equal to $\bar{\mathcal{C}}_c = 2/5$

¹⁵For the enhanced modes, it can be checked that, $\langle \{\delta\pi(\mathbf{k}), \delta\phi(\mathbf{k})\} \rangle \gg [\delta\pi(\mathbf{k}), \delta\phi(\mathbf{k})]$, so the correlation between field and momentum conjugate far exceeds the level of their intrinsic quantum uncertainty.

Eq.(2.38). Using this value, we can compute the mass spectrum following Eq.(2.39) and the abundance of the number of peaks Eq.(2.33). In particular, we compute $x_m(\mu_a) = r_m(\mu_a)k_{\text{max}}$ finding for each μ_a the corresponding location of the maximum of the compaction function $r_m(\mu_a)$ and taking into account the position of the maximum of the power spectrum $\mathcal{P}_{\zeta_G}(k_{\text{max}})$ for each realization of f_{NL} .

• Block III (bubble channel): Using $\Psi_b(N_\star, \tilde{r})$ computed from $\mathcal{P}_{\delta\phi}$, we set up the initial condition for bubble formation following the prescription of section 3. To solve numerically Eq.(3.1) we discretize it in the radial coordinate \tilde{r} using finite difference central scheme (second-order accuracy), and we use Runge-Kutta 4 method to evolve the equation in time. We also implement the following boundary conditions $\phi'(N, \tilde{r}=0) = \phi'(N, \tilde{r}=\tilde{r}_{\rm end}) = 0$ (where $'\equiv \partial/\partial \tilde{r}$ and being $\tilde{r}_{\rm end}$ the last point of the grid)¹⁶. In general, we have used $dN \sim 10^{-3.3}$ (time-step) with $d\tilde{r} \sim 10^{-3.6}$ (spatial-resolution) to evolve the equations. We solve the dynamics until the very end of inflation $N_{\rm end}$. At that time, we obtain the profile in $\phi(N,\tilde{r})$ from which we can infer the bubble size and study the tail profile of the scalar field, which will have important consequences on the mass function estimation as we will see in section 5.4. The threshold $\mu_{b,c}$ can be obtained through a bisection method, and repeating simulations with different values for $(\mu_b - \mu_{b,c})$, we can determine the size of the bubble in terms of the amplitude of the fluctuation.

Following the numerical procedure detailed above, we obtain parameters for the potential Eq.(2.2) fulfilling two criteria. First, in Table 1, we show parameters for which the threshold $\nu_{b,c} = \mu_{b,c}/\sigma_b$ takes three different values $\nu_{b,c} \sim 8, 10, 12$. This allows us to study the formation of the bubbles as a function of the threshold $\nu_{b,c}$. Second, in Table 2 we show parameters such that the total fraction of PBH in the form of DM is roughly one. For these parameters we can compute the mass function from the two channels of PBH production in a cosmologically relevant case.

In both cases we find iteratively the value of A fixing the other parameters values σ, ϕ_0, V_0 to fulfill the CMB constraints and have the peak k_{max} of the power spectrum \mathcal{P}_{ζ_G} at the asteroid mass range $M_k(k_{\text{max}}) \in [10^{-13}, 10^{-12}] M_{\odot}$ (see Table 1, 2 for details).

5 Numerical results

In this section we present the numerical results we have obtained following the procedures and techniques pointed out in the previous sections and using the parameters of Tables 1, 2.

5.1 Enhancement of cosmological fluctuations

The homogeneous solution of the inflationary dynamics of Eq.(2.4) is shown in Fig.3 for some specific values of $f_{\rm NL}$ following the Table 1, in particular for the case $\nu_{b,c} \sim 8$. The inflaton dynamics develops a plateau phase when the inflaton overshoots the barrier during a relatively small number of e-folds. The deceleration of the inflation is evident in the panel for $\dot{\phi}_{\rm bkg}(N)$, where the minimum velocity happens slightly before the inflaton approaches the maximum $\phi_{\rm max}$. The duration of this phase is smaller when increasing $f_{\rm NL}$. This is

¹⁶In discretizing the grid we have a limitation in implementing the boundary condition at infinity, which would be the ideal situation since $\phi(N, \tilde{r} \to \infty) = \phi_{\rm bkg}(N)$. We implement this condition at the last point of our grid at sufficiently large radii where the fluctuation $\Psi_b(N_\star, \tilde{r}_{\rm end})$ is very small compared with the background solution $\phi_{\rm bkg}(N)$.

due to the sharper profile of V around the local maximum of the barrier (see right panel of Fig.1). In the bottom panels of Fig.3 is shown the evolution of the ϵ_1 , ϵ_2 parameters. The corresponding deceleration of the inflation induces negative values in ϵ_2 .

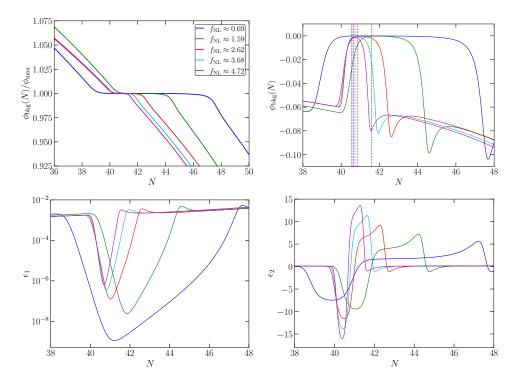


Figure 3. Top panels: Dynamics of the inflaton field $\phi(N)$ (left) and $\dot{\phi}_{\rm bkg}(N)$ (right) for different values of $f_{\rm NL}$. The dashed vertical lines indicates the location of $N_{\rm max}$, $\phi_{\rm bkg}(N_{\rm max}) \equiv \phi_{\rm max}$. Bottom panels: Evolution of the Hubble slow-roll parameters ϵ_1 (left), ϵ_2 (right) respectively for different $f_{\rm NL}$ values. In all cases, the parameters taken correspond to $\nu_{b,c} \sim 8$ from Table 1.

The power spectrum of the Gaussian curvature fluctuation \mathcal{P}_{ζ_G} obtained solving the MS equating is shown in Fig.4 for different $f_{\rm NL}$ values for the case $\nu_{b,c} \sim 8$. The large enhancement of the PS from the pivot scale $k = 0.05 {\rm Mpc^{-1}}$ to the PBH scales $(k_{\rm max} \in [10^{12}, 10^{13}] {\rm Mpc^{-1}})$ due to the significant reduction of $\dot{\phi}_{\rm bkg}$ is clear. The power spectrum \mathcal{P}_{ζ_G} becomes more monochromatic by increasing $f_{\rm NL}$, since the duration of the deceleration of the inflaton is smaller.

Notice that the peak amplitude $\mathcal{P}_{\zeta_G}(k_{\text{max}})$ decreases when we increase f_{NL} for the same fixed value $\nu_{b,c} \sim 8$, which is shown in the right panel of Fig.4. The same qualitative behaviour is found when fixing the fraction of PBHs to account for all the dark matter following the parameters of Table 2. For instance the peak $\mathcal{P}_{\zeta_G}(k_{\text{max}})$ is reduced by roughly a factor 5 when increasing f_{NL} from 1.59 to 3.92.

This is an interesting feature of non-gaussian models that can be exploited to avoid, for instance, spectral distortion constrains [79]. It is also relevant for the suppression of various non-gaussian contributions to some observables, as in the case of the induced gravitational waves [80], and could play a role in recent discussions of loop corrections to the power spectrum (see [81–84] and references therein). The reason behind the protection against non-Gaussian correction is simple. These contributions are typically proportional to $f_{\rm NL}^2 \mathcal{P}_{\zeta_G}(k_{\rm max})$. In the case of large $f_{\rm NL}$, when vacuum bubbles dominate, the critical am-

plitude for PBH production goes as $\mu_{a,c} \sim \nu_{a,c} \, \sigma_a \sim 1/f_{\rm NL}$ (since $\mu_{\star} \sim 1/f_{\rm NL}$ as shown in Eq.(2.23)). This implies that $f_{\rm NL}^2 \mathcal{P}_{\zeta_G}(k_{\rm max}) \sim f_{\rm NL}^2 \sigma_a^2 \sim \nu_{a,c}^{-2}$ is roughly independent on the non-Gaussianity parameter, and smaller than one.

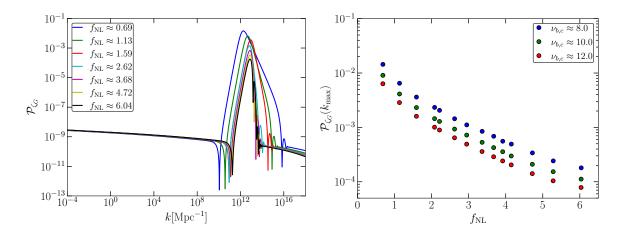


Figure 4. Left panel: Power spectrum of the Gaussian curvature fluctuation ζ_G for different values of $f_{\rm NL}$ for the case $\nu_{b,c} \sim 8$ (see Table 1). Right-panel: Reduction of the peak value of $\mathcal{P}_{\zeta_G}(k_{\rm max})$ in terms of $f_{\rm NL}$ for different values of $\nu_{b,c}$.

On the other hand, in Fig.5, we show the evolution of the curvatures modes ζ_G from the numerical solution of Eq.(2.9) in terms of the number of e-folds, for different representative modes k. The modes start with Bunch-Davies initial conditions well inside the cosmological horizon and freeze once they cross it at sufficiently large super-horizon scales. Qualitatively, modes that encounter a sufficiently large deceleration/acceleration of $\dot{\phi}_{\rm bkg}$ when they are roughly at horizon crossing can be enhanced/suppressed depending on the specific ratio aH/k. See [38] for a detailed description in terms of the MS equation with another type of inflationary model.

Finally in the right panel of Fig.5 we show the comparison of the numerical results with the analytical estimation of Eq.(2.12) (red line), where can be observed the underestimation of the enhancement from the assumption of the SR phase when computing the PS.

Making the anti-Fourier transformation of the power spectrum, we can obtain the twopoint correlation function $\Psi_a(\tilde{r})$ to build the full non-linear gaussian curvature fluctuation ζ . Then the compaction function C(r) can be obtained following Eq.(2.36) and using the numerical procedure of the averaged compaction function pointed out in section 4, we can finally obtain the threshold values $\mu_{a,c}$ for the collapse of the adiabatic fluctuation ζ . The result is shown in Fig.6.

This is similar to what was obtained in [1], with the difference that there were used numerical simulations with the code of [67] and taking an analytical approximation for the shape of the power spectrum. As already pointed out in that work, we observe a reduction of the threshold $\mu_{a,c}$ as the level of NGs increases. In the large $f_{\rm NL}$ limit, we observe that $\mu_{a,c} \to \mu_{\star}$. In this regime, it is expected that the production of PBHs from the adiabatic channel will decrease due to the proximity of the critical threshold $\mu_{a,c}$ to the limiting value μ_{\star} , which means that only a small range of allowed curvature fluctuations will be able to collapse forming PBHs. We will use $\mu_{a,c}$ to estimate the mass function and PBH mass in 5.4. Notice that the values are independent on $\nu_{b,c}$ since the threshold for PBH formation from

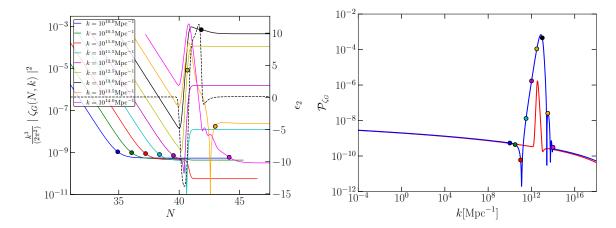


Figure 5. Left panel: Evolution of the modes ζ_G in terms of the number of e-folds N for some specific k modes. The solid dots indicate the time when the modes cross the cosmological horizon at $k=a(N_{\rm crossing})H(N_{\rm crossing})$. We show ϵ_2 as a dotted line. Notice that the modes that most contribute to the enhancement of \mathcal{P}_{ζ_G} become approximately frozen already at $N_\star\approx 41.18$, as given by the definition of Eq.(3.9). This is in agreement with the expected behaviour once the attractor regime sets in. This is not exact as for instance the black dot is not completely frozen at the asymptotic value. The effect is more dramatic for the orange and pink dots but these are very subdominant in the power spectrum. Right-panel: Power spectrum of \mathcal{P}_{ζ_G} obtained solving the MS equation (blue line) together with the one obtained using the analytical approximation of Eq.(2.12) (red line). The dots correspond to the values of k shown in the left panel. In both cases, we have considered the case $f_{\rm NL}\approx 3.68$ with $\nu_{b,c}\sim 8$.

the adiabatic channel $(\mu_{a,c})$ mainly depends on the shape around the critical compaction function's peak, as shown and discovered in [63].

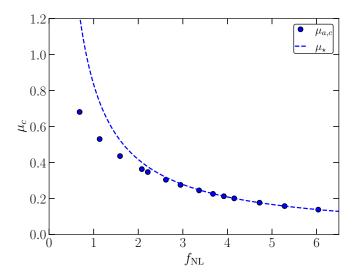


Figure 6. Threshold values $\mu_{a,c}$ obtained using the approach of the average of the compaction function (solid dots) in terms of the values $f_{\rm NL}$ and compared with the analytical values $\mu_{\star} = 5/(6f_{\rm NL})$ (dashed line).

Lets consider now the case of bubble formation. We first find the value of N_{\star} minimizing

the deviation $\Delta_{\rm att}(N_{\star})$ introduced in Eq.(3.9). We found that the attractor regime is fulfilled only approximately for a specific small range of e-folds. This approximation worsens when $f_{\rm NL}$ increases. This is shown in Fig.7, where the ratio $\dot{\phi}_{\rm bkg}/(\phi_{\rm bkg}-\phi_{\rm max})$ is plotted in terms of N. In the attractor regime we expect a constant flat plateau giving the value of $-\lambda_{-}$. This is satisfied approximately for small $f_{\rm NL}$, but for large $f_{\rm NL}$ there is no clear plateau. The deviation in percentage between the numerical solution and the attractor regime, which is a few per cent, is also displayed. For small $f_{\rm NL}$ the numerical results using the initial conditions Eqs.(3.6),(3.8) match the analytical estimates very well. For large $f_{\rm NL}$ Eq.(3.8) is less well justified but we still expect it to be a good approximation for modes which are exponentially growing near the top of the potential.

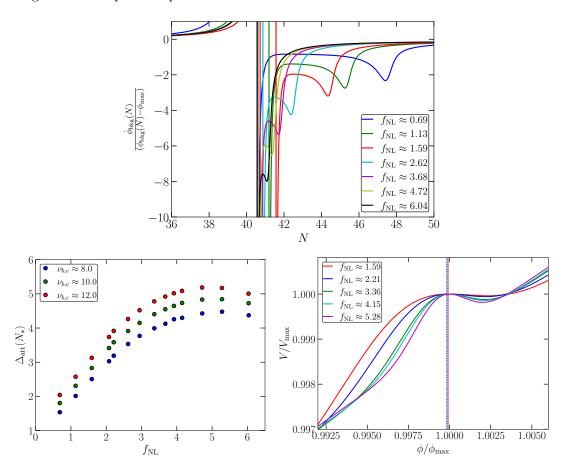


Figure 7. Top panel: Values of $\dot{\phi}_{\rm bkg}/(\phi_{\rm bkg}-\phi_{\rm max})$ in terms of the number of e-folds and for different $f_{\rm NL}$ for the case $\nu_{b,c}\sim 8$ (Table 1). Notice that in the attractor regime we expect a constant flat plateau giving the value of $-\lambda_-$. This plateau is well defined for small $f_{\rm NL}$ but gradually disappears for large $f_{\rm NL}$. Left-bottom panel: Deviation between the analytical attractor regime solution and the numerical one in percentage. Right-bottom panel: Shape of the potential for different $f_{\rm NL}$ and where the vertical dashed lines indicate the location of $\phi_{\rm bkg}(N_{\star})$ in V.

On the other hand, in Fig.8 it is shown the power spectrum $\mathcal{P}_{\delta\phi}$ evaluated at N_{\star} and reescaled with $\dot{\phi}_{\mathrm{bkg}}^2(N_{\star})$. At large scales k, the power spectrum matches with the power spectrum associated with the curvature fluctuation \mathcal{P}_{ζ_G} when we rescale it with the factor $\dot{\phi}_{\mathrm{bkg}}(N_{\star})$, since that modes k are already frozen at super-horizon scales when they are evaluated at N_{\star} . The local maxima we observe at short scales are attributed to the enhancement

of the perturbation field $\delta\phi$ due to the reduction of the inflaton velocity. In this case, not all modes have exited the cosmological horizon. At shorter scales than the local maxima, we find the expected growth of the curvature modes of the scalar field in a Minkowski vacuum $\sim k^2$, which corresponds to modes that are still inside the cosmological horizon. To take realistically into account the growth of the power spectrum, we take the limit of the integrals k_f and k_i from Eq.(3.5) such that the k_f corresponds to the local minima of $\mathcal{P}_{\delta\phi}$ after the local maxima, to avoid the unrealistic contribution from modes that are still growing within the cosmological horizon. The k_i is taken as the corresponding scale such that $\mathcal{P}_{\delta\phi}(k_f) = \mathcal{P}_{\delta\phi}(k_i)$ to account only for the enhancement due to the dynamics of the inflaton around the bump of V and avoid infrared contributions, which in any case wouldn't change the result taking into account the large enhancement of the $\mathcal{P}_{\delta\phi}$ at the peak compared with large scales.

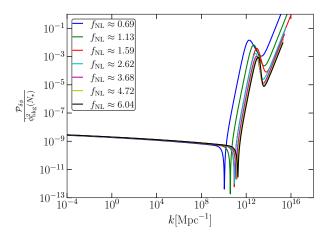


Figure 8. Power spectrum $\mathcal{P}_{\delta\phi}(N_{\star}, k)$ in units of $\dot{\phi}_{\mathrm{bkg}}^2(N_{\star})$ for different values of f_{NL} and the case $\nu_{b,c} \sim 8$ from the parameters in Table 1.

5.2 Bubble dynamics formation and size

Using the $\Psi_b(N_{\star}, \tilde{r})$ obtained numerically in the previous section allows us to build the initial conditions for bubble formation according to section 3 and then proceed to numerically solve the dynamical equation for the field $\phi(N, \tilde{r})$ Eq.(3.1).

An example of the dynamical formation of a bubble is shown in Fig.9 (panels in the top are for $\phi(N, \tilde{r})$ and in the bottom for $\dot{\phi}(N, \tilde{r})$), for the case $f_{\rm NL} \approx 2.62$ from Table 2 (other cases leads to a similar qualitative behaviour). We can make the following observations:

- In the left panel is shown a subcritical case $(\mu_b < \mu_{b,c})$, where the inflaton overshoots the barrier and exits inflation without the formation of bubbles. In this case, initially, the domain $\tilde{r} \gtrsim 0.5$ of the inflaton overshoots the ϕ_{max} , and therefore will exit inflation (notice also a negative velocity). On the other hand, for $\tilde{r} \lesssim 0.5$, the inflaton lies between the ϕ_{max} and ϕ_{min} of the potential with an initial small positive velocity, which makes the inflaton roll down to ϕ_{min} . After that, the contribution of the gradient of the scalar field and a negative velocity obtained when falling again into the minimum make the inflaton overshoot the barrier and avoid becoming trapped.
- In the middle panel, instead, is shown the evolution of the bubble formation for a supercritical case $(\mu_b > \mu_{b,c})$. In this case, the large backward quantum fluctuation

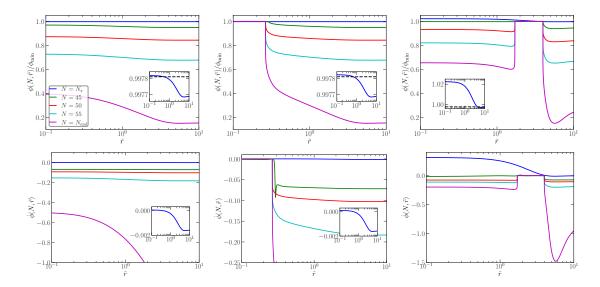


Figure 9. Profile of the inflaton at different e-folds N. Panels in the first row correspond to the evolution of $\phi(N,\tilde{r})$ in units of ϕ_{\min} , whereas in the second is shown the evolution of the velocity $\dot{\phi}(N,\tilde{r})$. Left panels corresponds to a subcritical case $\mu_b < \mu_{b,c} (\mu_b = \mu_{b,c} - 10^{-5})$, middle to super-ritical $\mu_b > \mu_{b,c} (\mu_b = \mu_{b,c} + 10^{-5})$ and right to super-supercritical $\mu_b \gg \mu_{b,c} (\mu_b = \mu_{b,c} + 10^{-1})$. The three cases correspond to the case $f_{\rm NL} \approx 2.62$ from Table 2 with $\mu_{b,c} \approx 5.243 \cdot 10^{-4}$. The subplots show the initial configuration at N_{\star} for better visualization. In particular, the dashed line corresponds to $\phi_{\rm max}$ in units of $\phi_{\rm min}$.

is sufficiently large to trap a localized region of the inflaton field, producing the false vacuum bubble. The size of the bubble is defined as the last point of the comoving size \tilde{r} such that fulfil $\phi(N_{\rm end}, \tilde{r} \leq R_{\rm b}) = \phi_{\rm min}$ (being R_b the size of the bubble in units of $1/(a(N_\star)H(N_\star))$), since the region where the inflaton is trapped will correspond to the minima of V and the field domain that exits the barrier will fulfill $\phi(N_{\rm end}, \tilde{r} > R_b) < \phi_{\rm max}$. Notice that for $\dot{\phi}(N_{\rm end}, \tilde{r} \leq R_b)$, the velocity is zero since the inflaton is trapped. Interestingly, at the end of inflation, there is a tail for the scalar field, which doesn't precisely correspond to a domain wall shape. We will comment on that in more detail later on.

• In the right panels, we have a super-supercritical fluctuation with $\mu_b \gg \mu_{b,c}$. We find the formation of a concentric shell instead of a central bubble. In this case, at N_{\star} , the large backward quantum fluctuation will displace the central region of the inflation far away from the minima ϕ_{\min} allowing this region to get enough velocity when falling again into the minima to, after that, overshoot the barrier. Instead, the tail that falls between ϕ_{\min} and ϕ_{\max} will become trapped similarly as in the previous case. Although this last scenario has an interesting dynamical behaviour, as we will see later on, such a case is largely statistically suppressed since $\mu_b \gg \mu_{b,c}$. Therefore, in this work, we will only consider standard spherically-centred bubbles.

Using a bisection method, we obtain the thresholds $\mu_{b,c}$, which can be seen in Fig.10 for different $\nu_{b,c}$. In the left panel of Fig.10 $\mu_{b,c}$ increase in terms of $f_{\rm NL}$, which is in agreement with the fact that the distance between the point where we implement the initial condition $\phi_{\rm bkg}(N_{\star})$ and the position of the maximum of the potential $\phi_{\rm max}$ (see right panel) increases with $f_{\rm NL}$ up to remain roughly constant, and therefore the amplitude of the backward fluctu-

ation should be larger to make the inflaton trapped. Another effect in combination with the previous one is that the shape of V around ϕ_{max} is sharper for larger f_{NL} , then the gradients of V increase the minimum μ_b needed to make the inflaton trapped and produce the bubble, due to the forces of the potential in the inflationary dynamics.

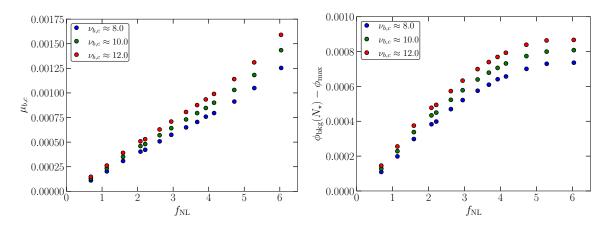


Figure 10. Left panel: Threshold $\mu_{b,c}$ in terms of $f_{\rm NL}$ and for different $\nu_{b,c}$. Right panel: Difference in the field ϕ between the location of N_{\star} and $\phi_{\rm max}$ in terms of $f_{\rm NL}$ and for different configurations $\nu_{b,c}$. The parameters chosen correspond to Table 1.

By making simulations for small values of $\mu_b - \mu_{b,c}$, we can explore the critical regime of the bubble sizes. This is shown in Fig.11 for a specific case of $\nu_{b,c} = 8$. We have found for this case that for fluctuations very close to the critical one with $\mu_b - \mu_{b,c} \lesssim 10^{-1} \mu_{b,c}$ the bubble size follows a critical regime¹⁷

$$R_b(\mu_b) = \mathcal{K}_b(\mu_{b,c})(\mu_b - \mu_{b,c})^{\gamma_b(f_{\rm NL})},\tag{5.1}$$

where K_b is a constant that depends on the threshold $\mu_{b,c}$ for each configuration $f_{\rm NL}$ and γ_b (shown in Fig.12) seems to be in general a coefficient independent on the threshold $\mu_{b,c}$, and only dependent on $f_{\rm NL}$. For small $f_{\rm NL}$, the critical exponent saturates to a factor ~ 0.50 , but then starts to increase for $f_{\rm NL} \gtrsim 2$. Due to a limitation of the resolution $d\tilde{r} \sim 10^{-3.6}$ (this mainly induces the error bars in the coefficient γ_b shown in the figure), we cannot make simulations for very small $\mu_c - \mu_{b,c}$ to explore the bubble size for large $f_{\rm NL}$ since R_b becomes smaller. In any case, we expect that the critical regime Eq.(5.1) should hold for smaller $\mu_b - \mu_{b,c}$ than the ones tested, as it is more clearly shown for small $f_{\rm NL}$ where the bubble size is larger, and the critical regime is clearly identified. Still, a dedicated study with some specific technique like adaptive mesh refinement [86, 87] would probably be needed to confirm our intuition, specially for the cases of large $f_{\rm NL}$ where the simulations are more challenging.

Physically the spread in bubble sizes can be understood as follows. A small fluctuation with $\mu_b < \mu_{b,c}$ may form a very small bubble, but that one immediately recollapses under its tension and leaves nothing behind. The bubble with $\mu_b = \mu_{b,c}$, on the other hand, will

¹⁷This is reminiscent of the critical behaviour in gravitational collapse [85]. However, the present case is a different phenomenon where gravitational forces do not play a role.

¹⁸The differences on $\gamma_b(f_{\rm NL})$ between the three cases tested $\nu_{b,c} \approx 8, 10, 12$ considered in Table 1 lies within the error bars. For $f_{\rm NL} \lesssim 2$, where the precision for the exponent is quite high, we find indeed that the exponent is independent on ν_b . We expect that this characteristic also hold for larger $f_{\rm NL}$, and it only should depend on the shape of V around $\phi_{\rm max}$, which characterizes $f_{\rm NL}$ through Eqs.(2.21),(2.23).

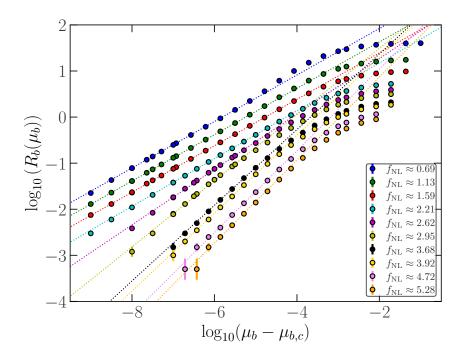


Figure 11. Size of the bubbles in logarithmic scale for different amplitudes $\mu_b - \mu_{b,c}$ for the case $\nu_{b,c} = 8$. The dashed lines indicate Eq.(5.1) with the fitting done in the range where the scaling law is more likely with $\mu_b - \mu_{b,c} \lesssim 10^{-1} \mu_{b,c}$. There are also shown the error bars due to the resolution of the grid.

be in unstable equilibrium between expansion and recollapse. Classically, it could stay in this "loitering" equilibrium point, with a fixed physical size, for an indefinite number of e-foldings before it decides to expand or recollapse. The longer the bubble is loitering, the smaller will be the co-moving size of the bubble. That is the reason why we have a tail of smaller co-moving size bubbles as the critical amplitude is approached.

In practice, however, we have to account for the fact that, while the bubble is loitering, quantum fluctuations of the field will keep accumulating, changing in practice the overall amplitude μ of the original field perturbation. The field fluctuates by the amount $(\delta\phi)^2 \sim (H/2\pi)^2$ per e-folding, and over a period ΔN such fluctuations add quadratically as a random walk, so we have

$$\Delta \mu \sim \frac{H}{2\pi} (\Delta N)^{1/2} \gtrsim (\mu_b - \mu_{b,c}). \tag{5.2}$$

The last inequality is meant to represent the boundary beyond which the fluctuation in the amplitude is large enough to make the bubble recollapse. Since the co-moving size of the bubble follows the scaling $R_b \sim e^{-\Delta N}$, for any given R_b the relation (5.2) leads to a minimum amplitude $\mu_{b,(\text{cut-off})}$ above $\mu_{b,c}$, such that the required amount of loitering is still allowed by the quantum drift:

$$\mu_{b,(\text{cut-off})} - \mu_{b,c} \approx \sqrt{-\ln(R_b(\mu_b))} \frac{H(N_\star)}{2\pi}.$$
 (5.3)

This represents a quantum boundary of the classical scaling regime.

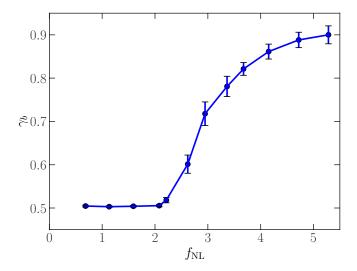


Figure 12. Critical exponent γ_b of the size of the bubbles $R_b(\mu_b)$ in terms of the non-Gaussian parameter $f_{\rm NL}$. There are also indicated error bars from the numerical fitting of the data to Eq.(5.1), mainly due to grid resolution limitation and the specific range of $\mu_b - \mu_{b,c}$ chosen where the fit is performed.

Finally, we have found that at the end of inflation¹⁹, the bubble is surrounded by a tail of the scalar field ϕ , as is shown in Fig.13 for different values $\mu_b - \mu_{b,c}$. This tail is more important for values μ_b closer to the critical $\mu_{b,c}$. Making use of the δN formalism, we can compute the contribution of the curvature fluctuation from the tail ζ_{tail} as $\zeta_{\text{tail}} \equiv \delta N$ with $\phi(N_{\text{end}}, \tilde{r}) = \phi_{\text{bkg}}(N_{\text{end}} - \delta N)$. The profiles ζ_{tail} are shown in the right panel of Fig.13.

Remarkably, we find that $\zeta_{\rm tail}$ is indeed a fluctuation of type-II, which fulfills that $1 + \tilde{r}_{\rm tail}\zeta'(\tilde{r}_{\rm tail}) = 0$ and the scale $\tilde{r}_{\rm tail}$ is indicated as a dot in the Fig.13. What we will see in section 5.4 is that, indeed, the $\zeta_{\rm tail}$ will dominate the final PBH mass with respect to the contribution of the bubble itself. We have observed that the $\tilde{r}_{\rm tail}$ seems to follow a scaling law in terms of the amplitude $\mu_b - \mu_{b,c}$ as $\tilde{r}_{\rm tail} \sim (\mu_b - \mu_{b,c})^{\gamma_{\rm tail}}$ (similar to Eq.(5.1)) for the cases tested in Table 2. We leave for future research a more detailed exploration of that.

5.3 PBH production from the adiabatic and bubble channel

In the left panel of Fig.14, we show the numerical results for the thresholds ν_c for both channels of production. We choose three values for $\nu_{b,c} \approx 8, 10, 12$, and with these parameters we compute the corresponding normalised threshold $\nu_{a,c}$ for the adiabatic channel. We also show the analytical estimate $\nu_{\star} = 5/(6f_{\rm NL})$. In the case of small NGs, the values of the analytical estimate for the bubble channel ν_{\star} match with very good agreement with the numerical one $\nu_{b,c}$, being $\nu_{a,c}$ smaller. Instead $\nu_{a,c}$ increases with $f_{\rm NL}$ for given value of $\nu_{b,c}$. For $f_{\rm NL} \approx 2.6$, $\nu_a > \nu_b$, meaning that bubble formation becomes more likely than PBH formation through the adiabatic channel. Let us note that $\nu_{b,c}$ starts to differ from the analytical estimate ν_{\star} , meaning that bubble formation is more likely than previously

¹⁹Notice that we are considering a homogeneous Hubble factor in Eq.(3.1) since we are not including the backreaction to the spacetime metric. This would make a minor correction on the final profile of the scalar field at the end of inflation, where the friction due to the backreaction is not considered, and therefore the ζ_{tail} could be slightly underestimated. We leave for future research a refinement on that to take into account this possible small correction.

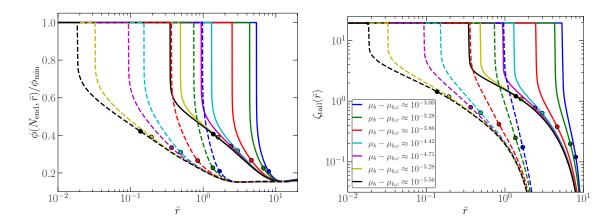


Figure 13. Left-panel: Profile of the inflaton $\phi(N, \tilde{r})$ at the end of inflation $N_{\rm end}$. Right panel: adiabatic curvature fluctuation $\zeta_{\rm tail}$ that surrounds the scalar field obtained using the δN formalism. In both cases, the solid line is the case for $f_{\rm NL} \approx 1.59$ and dashed for $f_{\rm NL} \approx 2.95$ from Table 2. The dots show the location $\tilde{r}_{\rm tail}$ for what $1 + \tilde{r}_{\rm tail}\zeta'_{\rm tail}(\tilde{r}_{\rm tail}) = 0$ (notice that we reescaled r in terms of \tilde{r} in the numerical simulations). The different colours represents different cases of $\mu_b - \mu_{b,c}$.

estimated. Notice that this qualitative behaviour is the same for the different values of $\nu_{b,c}$ chosen. In the right panel instead, we show the thresholds μ_c for the adiabatic channel

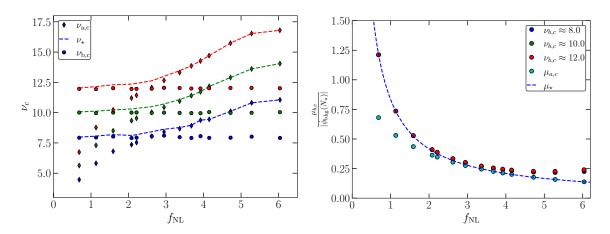


Figure 14. Left-panel: Critical values ν_c for the two channels of PBH formation. Circles represents the thresholds for the bubble channel $\nu_{b,c}$, thin diamond the adiabatic channel $\nu_{a,c}$ and the dashed line the analytical estimate $\nu_{\star} = 5/(6f_{\rm NL})$. Right-panel: Values $\mu_{b,c}/|\dot{\phi}_{\rm bkg}(N_{\star})|$ compared with the analytical μ_{\star} and the numerical values $\mu_{a,c}$. In both panels, blue, green and red symbols correspond to the cases $\nu_{b,c} \sim 8, 10, 12$ respectively.

compared with the normalized threshold of the bubble channel in units of $|\phi_{\rm bkg}(N_{\star})|$. The values for the bubble channel match with very good agreement with the ones inferred from the analytical estimate for small $f_{\rm NL}$, but we start to see a deviation for larger $f_{\rm NL} \gtrsim 3$. Notice that although we find for large $f_{\rm NL}$ that $\mu_{b,c}/|\dot{\phi}_{\rm bkg}(N_{\star})| > \mu_{a,c}$, in the left panel we have $\nu_{b,c} < \nu_{a,c}$. We should take into account that the integrated power spectrum is larger for $\mathcal{P}_{\delta\phi}/|\dot{\phi}_{\rm bkg}(N_{\star})|$ than for \mathcal{P}_{ζ_G} . Therefore $\sigma_b/|\dot{\phi}_{\rm bkg}(N_{\star})| > \sigma_a$, making the bubble-channel for PBH formation more likely. We can then estimate the relative abundance of the peaks

generated by the adiabatic fluctuations and the bubbles using the values of Fig.14 following the procedure of section 2.4. The abundance of the number of peaks from both channels is estimated as

$$\beta_{a} = \int_{\nu_{a,c}}^{\nu_{\star}} \mathcal{N}_{a}(\nu_{a}) d\nu_{a} = \int_{\nu_{a,c}}^{\nu_{\star}} \left(\frac{\sigma_{a,1}}{\sqrt{3}\sigma_{a,0}} \right)^{3} (\nu_{a}^{3} - 3\nu_{a}) e^{-\frac{1}{2}\nu_{a}^{2}} d\nu_{a}, \tag{5.4}$$

$$\beta_{b} = \int_{\nu_{b,c}}^{\infty} \mathcal{N}_{b}(\nu_{b}) d\nu_{b} = \int_{\nu_{b,c}}^{\infty} \left(\frac{\sigma_{b,1}}{\sqrt{3}\sigma_{b,0}} \right)^{3} (\nu_{b}^{3} - 3\nu_{b}) e^{-\frac{1}{2}\nu_{b}^{2}} d\nu_{b}.$$
 (5.5)

Notice that we are considering that the limits of integration for both cases are different. In the adiabatic channel, we integrate from $\nu_{a,c}$ (obtained using the analytical approach of the averaged compaction function) to the limiting value ν_{\star} for which the log-template relation is defined. On the other hand, in the bubble channel, we integrate from $\nu_{b,c}$ up to infinity. In Fig.15 we show the ratio $\beta_{\rm a}/\beta_{\rm b}$ in terms of the value of $f_{\rm NL}$.

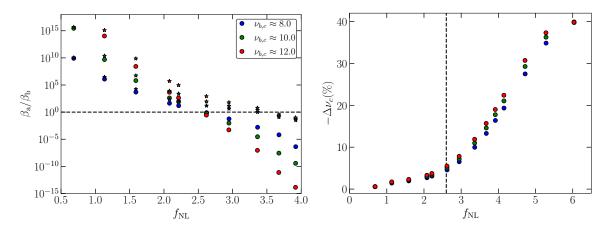


Figure 15. Left panel: Relative abundance between the number of peaks generated from the adiabatic and the bubble channel. Dots represent the results of numerical simulations using $\nu_{b,c}$, whereas the stars are computed using the analytical value ν_{\star} . Right-panel: Relative deviation $\Delta\nu$ between the numerical $\nu_{b,c}$ and analytical estimate ν_{\star} in percentage defined in Eq.(5.6), in terms of $f_{\rm NL}$ and for different fixed values of $\nu_{b,c}$.

We find that the number of peaks generated by the bubble channel dominates over those coming the adiabatic one for $f_{\rm NL} \gtrsim 2.6$, being $f_{\rm NL} \approx 2.6$ (dots in the figure) the commensurable case with $\beta_a \approx \beta_b$. We also show the values computed considering the analytical estimate of ν_{\star} (star symbol) in the computation of Eq.(5.4). The latter underestimates the production of bubbles at higher $f_{\rm NL}$. In particular for the case $f_{\rm NL} \approx 3.5$ bubbles are already $\sim 10^3$ more abundant by comparison.

On the other hand, in the right panel of Fig.15, we show the relative deviation in percentage between $\nu_{b,c}$ and the analytical estimate ν_{\star} that we expect from the log relation between ζ_G and ζ (Eq.(5.6)). We define the relative deviation $\Delta\nu_c$ as

$$\Delta\nu_c(\%) = 10^2 \frac{\nu_{b,c} - \nu_{\star}}{\nu_{b,c}}.$$
 (5.6)

We find good agreement between the analytical estimate ν_{\star} and the numerical result $\nu_{b,c}$ for small $f_{\rm NL}$. This is the regime where we precisely expect that the analytical estimate

should be more accurate, as mentioned in section 2.3. Increasing $f_{\rm NL}$ the deviation $\Delta \nu$ is larger, which could be due to several reasons. First of all, for large $f_{\rm NL}$ the attractor solution in the quadratic part of the potential (see Fig.7) is lost, and therefore we are not in the regime of applicability of Eq.(2.20). Another reason may be the use of initial conditions $\delta \dot{\phi}_{\rm bkg} = -\lambda_- \delta(\phi_{\rm bkg} - \phi_{\rm max})$ at N_\star , again corresponding to the attractor regime. Even so, the deviation $\Delta \nu_c$ is within a factor $\sim 12\%$ for $f_{\rm NL} < 3.5$. A more realistic comparison between ν_\star and $\nu_{b,c}$ for very large values of $f_{\rm NL}$ would require new methods and is left for future research.

5.4 Mass function and spectrum of PBHs

In this last section, we are going to use the numerical results to estimate the mass function and spectrum from both channels of PBH production. The PBH mass spectrum of the adiabatic channel follows the critical regime when $\nu_a \to \nu_{a,c}$ as already shown in Eq.(2.39)

$$M_a(\nu_a) = \mathcal{K}_a \sigma_a^{\gamma_a} x_m^2(\nu_a) e^{2\zeta(r_m(\nu_a))} (\nu_a - \nu_{a,c})^{\gamma_a} M_k(k_{\text{max}}), \tag{5.7}$$

where $x_m(\nu_a) = k_{\text{max}} r_m(\nu_a)$ being k_{max} the location of the peak of the power spectrum \mathcal{P}_{ζ_G} . Then, the mass function contribution from the adiabatic channel is estimated using peak theory following [68, 88]

$$f_{\rm a}(M_a) = \frac{M_{\rm a}(\nu_a)\mathcal{N}_{\rm pk}(\nu_a(M_a))}{\rho_{\rm critical}\Omega_{\rm DM}} \left| \frac{d\ln M_a(\nu_a)}{d\nu_a} \right|^{-1},\tag{5.8}$$

where $\rho_{\text{critical}} = 3M_{\text{pl}}^2 H_0^2$ corresponds to the current critical energy density of the Universe and Ω_{DM} the current fraction of dark matter. The last term in Eq.(5.8) is the inverse of the Jacobian, which in the critical regime is given by,

$$\frac{d\ln M_a(\nu_a)}{d\nu_a} = \frac{2}{x_m(\nu_a)} \frac{dx_m(\nu_a)}{d\nu_a} + 2\frac{d\zeta(r_m(\nu_a))}{d\nu_a} + \frac{\gamma_a}{\nu_a - \nu_{a,c}}.$$
 (5.9)

When $\nu_a \to \nu_{a,c}$ the Jacobian is dominated by the last term and therefore $f_a(M_a) \sim M_a^{1+1/\gamma_a}$. The contribution to the mass function for the bubble channel needs to take into account several considerations.

As we have mentioned, there is a surrounding adiabatic curvature fluctuation of type-II at the end of inflation ζ_{tail} . This fluctuation will source the main contribution to the PBH mass in comparison with the bubble itself, since the length-scale \tilde{r}_{tail} can be substantially larger than the comoving scale of the bubble size R_b . Once the baby Universe becomes causally disconnected from the parent Universe (see Fig.4 of [22] and Fig.3 of [89] for a schematic picture of the inflating bubble and a causal diagram respectively) the fluctuation of type-II will be swallowed by the remaining event horizon. Notice that although the PBH mass contribution from the bubble channel is dominated by fluctuations of type-II, its dynamical formation is completely different from the standard adiabatic channel, due to the presence of the bubble.

In order to obtain a very accurate estimation of the resulting PBH mass, it would be necessary to perform a full numerical simulation to take into account the full shape of $\phi(N_{\rm end}, \tilde{r})$ including the $\zeta_{\rm tail}$, which is left for future research. But we can already make a realistic estimation taking into account only the contribution to the PBH mass from the $\zeta_{\rm tail}$, which will give the dominant contribution. Fluctuations of type-II have not been explored

numerically yet, and its precise mass spectrum is unknown (although one expects larger masses than type-I since they are fluctuations highly over-threshold). But as a first estimate following the common consideration done for fluctuations of type-I²⁰, we will mainly consider that the PBH mass formed is basically the horizon mass when the comoving scale $r_{\rm tail}$ reenters the cosmological horizon. Specifically

$$M_b(\nu_b) = FM_k(k_{\text{tail}}(\nu_b)), \tag{5.10}$$

where the $k_{\text{tail}}(\nu_b)$ wave-mode is given by

$$k_{\text{tail}}(\nu_b) = \frac{1}{r_{\text{tail}}(\nu_b)e^{\zeta_{\text{tail}}(r_{\text{tail}}(\nu_b))}}.$$
 (5.11)

Notice its dependence with the amplitude ν_b according to Fig.13. In other words, the location of the peak of the compaction function will depend on the amplitude of the fluctuation ν_b that generates the bubble. The constant factor F relates the comoving size at horizon crossing with the mass of the resulting black hole. In most PBH formation scenarios this factor is of the order of a few. Numerical simulations would be required to determine it with precision, which is outside the scope of the present work. The numerical result of [21, 89] found that the PBH mass formed from large vacuum bubbles is basically the horizon mass at the time when the comoving scale of the bubble reenters the cosmological horizon times a factor F=5.6. That case is different from ours since we find the surrounding adiabatic curvature fluctuation $\zeta_{\rm tail}$ at the tail of the bubble profile instead of a perfect domain wall profile. Although that, we expect that the value F will be similar in a range (1-10), and we propose a factor $F\sim 3$ instead of 5.6 to account for this possible variation.

In the top-left panel of Fig.16, we show the mass dependence of both channels of PBH production in terms of the amplitude μ . The mass increases in both cases, although in the adiabatic channel there is a reduction for very large μ_a , consistent with the sharp reduction of the \tilde{r}_m (since the compaction function becomes compressed towards the origin of coordinates) shown in the right-top panel. Notice that the PBH mass in the case of the adiabatic channel is substantially smaller than the bubble channel for very small $\mu_a - \mu_{a,c}$ due to the effect of the critical regime. Moreover \tilde{r}_{tail} increases when stronger backward quantum fluctuations are considered, which can also be visualized in Fig.13. We also show the compaction functions in the bottom panel for the case $\mu - \mu_c \approx 10^{-4}$. As expected, the peak value of $C_{\zeta_{\text{tail}}}$ is located at 2/3 (the maximum value) since it corresponds to type-II fluctuation. In this case for fluctuations of type-II, should exist another local maximum with peak value 2/3, which is hidden inside the bubble and matches with the location of the bubble size R_b .

Then, the mass function for PBHs from the bubble channel is given by

$$f_{\rm b}(M_b) = \frac{M_b \mathcal{N}_{\rm pk}(\nu_b(M_b))}{\rho_{\rm critical} \Omega_{\rm DM}} \left| \frac{d \ln M_b(\nu_b)}{d\nu_b} \right|^{-1}, \tag{5.12}$$

where the Jacobian term in this case is computed as

$$\frac{d\ln M_b(\nu_b)}{d\nu_b} = \frac{2}{r_{\text{tail}}(\nu_b)} \frac{dr_{\text{tail}}(\nu_b)}{d\nu_b} + 2\frac{d\zeta_{\text{tail}}(r_{\text{tail}}(\nu_b))}{d\nu_b}.$$
 (5.13)

²⁰In the appendix A, we make another estimate to take into account the possible effect of accretion using the average of the compaction function. The result does not differ substantially from the one we consider in this section.

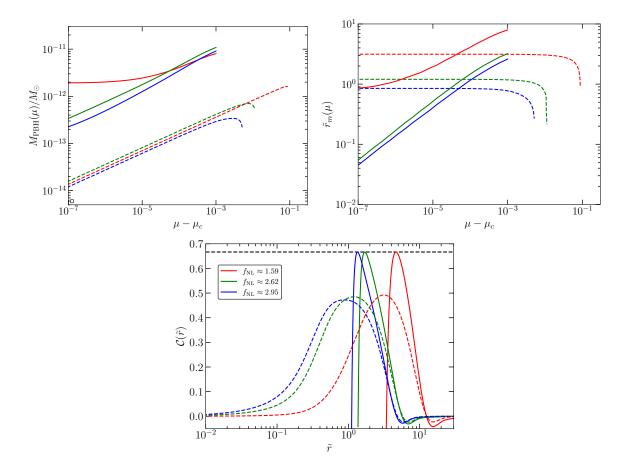


Figure 16. Top-Left panel: PBH mass dependence in terms of the amplitude of the fluctuation μ . In both cases, the amplitude μ corresponds to the adiabatic (dashed-line) and bubble channel (solid-line) corresponds to μ_a and μ_b , respectively. This also holds for the other plots. Top-Right panel: location \tilde{r}_m of the peak of the compaction function from the ζ_{tail} and the one from ζ in terms of the amplitude μ . Bottom panel: compaction functions from the bubble channel ζ_{tail} and from the standard adiabatic fluctuation ζ for different cases of f_{NL} and with a fixed $\mu - \mu_c \approx 10^{-4}$.

The total fraction of PBHs in the form of dark matter taking into account both channels of PBH production is simply given by

$$f_{PBH}^{\text{tot}} = \int_{-\infty}^{\infty} f_a(M_a) d\log M_a + \int_{-\infty}^{\infty} f_b(M_b) d\log M_b.$$
 (5.14)

The result for the mass function²¹ is shown in Fig.17, which is compared with the current observational constraints²² of PBHs in the form of dark matter in this mass range (see the

²¹Notice that for visualization purposes, we have only considered the mass spectrum before the decrease shown in Fig.16 to avoid the apparent divergence from the Jacobian in Eq.(5.8) (similar consideration was done in [68]), which is integrable and hardly contributes to $f_{\rm PBH}^{\rm tot}$. In Table 2, we give the values of $f_{\rm PBH}^{\rm tot}$ taking into account the full range $\mu_{a,c} < \mu_a < \mu_{\star}$. Notice as well that we are assuming that the scaling law Eq.(5.7) is fulfilled even for very large amplitudes up to $\mu_a < \mu_{\star}$, for what can be deviated few percentages as shown in [67], and therefore this apparent divergent feature may not be found if numerical simulations are used to study the mass spectrum for very large μ_a .

²²The constraints assume a monochromatic mass function, which is not strictly our case. Nevertheless we follow the standard practice in the literature to get an orientative plot.

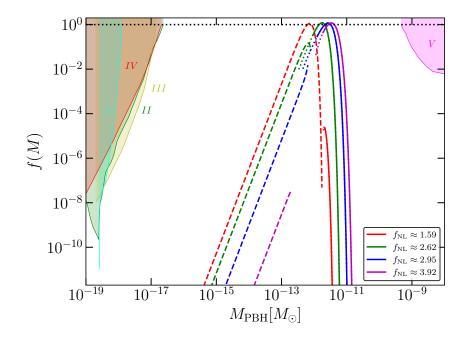


Figure 17. Mass function f(M) for the two channels of PBH production: false vacuum bubbles (solid line) and adiabatic channel (dashed line) in terms of different values of $f_{\rm NL}$. The mass range of f(M) for the case $f_{\rm NL}\approx 2.95$ (blue line) and $f_{\rm NL}\approx 3.92$ (magenta line) has been shifted by a factor $\sim 2-4$ respectively for visualization purposes. The constraints of the fraction of PBHs in the form of dark matter are also shown, which have been obtained by digitalizing Fig.11 of [12]. Constraint I comes from Galactic γ -rays [90], II from extragalactic γ -rays [91], III from Voyager-1 e^{\pm} [92], IV from CMB spectral distortions and anisotropies [93, 94] and V from from microlensing of stars in M31 by Subaru (HSC) [95]. See [12] for more details. The dotted lines correspond to values $\mu_b < \mu_{b,({\rm cut}-{\rm off})}$, which are included for completeness, but are not taken into account when normalizing the mass function. In particular, the corresponding cut-off for μ_b according to Eq.(5.3) is given by $\mu_{b,({\rm cutoff})} - \mu_{b,c} \approx 1.32 \cdot 10^{-6}$ (for $f_{\rm NL} \approx 1.59$), $\mu_{b,({\rm cutoff})} - \mu_{b,c} \approx 1.66 \cdot 10^{-6}$ (for $f_{\rm NL} \approx 2.62$), $\mu_{b,({\rm cutoff})} - \mu_{b,c} \approx 1.81 \cdot 10^{-6}$ (for $f_{\rm NL} \approx 2.95$) and $\mu_{b,({\rm cutoff})} - \mu_{b,c} \approx 2.22 \cdot 10^{-6}$ (for $f_{\rm NL} \approx 3.92$).

line) dominates over the adiabatic (dashed line). Since the contribution from the bubble channel is dominated by a fluctuation of type-II whereas in the adiabatic channel the main contribution comes from fluctuations of type-I, we show that fluctuations of type-II can contribute substantially more to the mass function than the standard fluctuations of type-I. To our knowledge, this is the first example where this behaviour has been noted.

Notice that in the adiabatic channel we can also have a spectrum of fluctuations of type-II for relatively small $f_{\rm NL}$ (for sufficiently large $f_{\rm NL}$ it is not possible to have fluctuations of type-II within a range of amplitudes $\mu_{a,c} < \mu_a < \mu_{\star}$). However, within our considerations and for the cases tested these fluctuations are statistically highly suppressed compared with fluctuations of type-I. The main point is that we should consider the bubble channel of PBH production together with the adiabatic one. Finally, in the case when both channels give a commensurable production of PBHs, accounting for the contribution of the bubble channel makes the mass function significantly broader.

6 Conclusion and discussion

In this work, we have numerically studied the vacuum bubble formation process produced by trapping a localized region of the inflaton field, due to large backward fluctuations after it overshoots a bump in a single field Starobinsky potential. These bubbles represent a second channel for the production of PBHs and might coexist with PBHs created from the collapse of large adiabatic perturbations.

Using numerical simulations with consistent initial conditions, we have found the threshold for the creation of these bubbles, and thus, we have been able to accurately predict the relative abundance of adiabatic PBHs versus bubble PBHs. This can be expressed in terms of the strength of non-Gaussianity $f_{\rm NL}$, which parametrizes a local relation between the curvature perturbations ζ and the Gaussian variable ζ_G Eq.(2.20).

Our results in the limit of small $f_{\rm NL}$ confirm that the log relation between the Gaussian curvature fluctuation and its non-Gaussian counterpart in the presence of a small bump is successful in predicting the channel of bubble formation, which is remarkably accurate within a deviation of 5% for $f_{\rm NL} \lesssim 2.6$. For larger $f_{\rm NL} \gtrsim 3.5$, the numerical results deviate more from the analytical estimate. This is to be expected, since in this regime the assumption of reaching the attractor in the quadratic part of the potential becomes less accurate (see caption of Fig.5). It would be interesting to see whether this feature is model-independent or not.

We have confirmed the result found in [1] that the number of peaks generating the bubbles is higher than those producing adiabatic PBHs in the case of large non-Gaussianity. Specifically we find that this happens for $f_{\rm NL} \gtrsim 2.6$ as shown in Fig.14. This is slightly smaller than the value $f_{\rm NL} \approx 3.5$ found in [1], indicating that vacuum bubbles are more easily formed than expected. The reason is a slight evolution of the power spectrum from the time N_{\star} when bubbles form to the end of inflation, where adiabatic perturbations will set in.

On the other hand, we have found for the cases tested that the comoving size of the bubble at the end of inflation follows a critical regime for sufficiently small $\mu_b - \mu_{b,c}$ with a critical exponent γ_b that increases for larger values of $f_{\rm NL}$. This makes the size of the bubbles significantly smaller for very small $\mu_b - \mu_{b,c}$ when considering models with large $f_{\rm NL}$. Even so, a numerical refinement method would be needed to reduce the error bars in Fig.12 and explore the bubble size behaviour for smaller values $\mu_b - \mu_{b,c}$, especially for large $f_{\rm NL}$.

Interestingly, at the end of inflation, the bubble is surrounded by an adiabatic curvature fluctuation ζ_{tail} , which surprisingly has been found to be of type-II. To the best of our knowledge, this is the first example where it is explicitly shown that fluctuations of type-II contribute substantially more to the PBH abundance than standard fluctuations of type-I. This is explicitly shown in the mass function f(M) of Fig.17, which for small f_{NL} is dominated by fluctuations of type-I (adiabatic channel) and for large f_{NL} it is dominated by fluctuations of type-II (bubble channel). A refinement of the PBH mass function with full simulations that take into account the gravitational collapse of fluctuations of type-II is left for future research.

Finally, we have shown explicitly that, for a given abundance of PBHs, the amplitude of the peak of the power spectrum needs to be smaller as $f_{\rm NL}$ increases. In this work, we have chosen the parameters of the inflationary potential to realize a peak in the power spectrum in the asteroid mass range, for which there are currently no strong constraints, and there is compatibility for PBHs to account for all the dark matter. Still, it would be interesting to

repeat the same analysis in the mass range of stupendous massive black holes [79, 96, 97], where there are relatively strong constraints (see Figs.37,19 of [7, 12] respectively) due to μ distortions from the CMB [98]. Therefore, large non-gaussianities can help avoiding the restriction on the power spectrum peak amplitude [99, 100], even when there is a sizable fraction of dark matter in the form of PBH. Such fraction will in fact come from the bubble channel of PBH production.

Acknowledgments

We thank Ken-ichi Nakao, Chulmoon Yoo and Hirotaka Yoshino for discussions about vacuum bubbles. A.E. acknowledges support from the JSPS Postdoctoral Fellowships for Research in Japan (Graduate School of Sciences, Nagoya University). J.G. is supported by the Unit of Excellence MdM 2020-2023" award to the Institute of Cosmos Sciences (CEX2019-000918-M) and by grants AGAUR 2021-SGR00872, PID2019-105614GB-C22.

A Possible effect of mass accretion

We have made another estimation using the averaged $\bar{\mathcal{C}}$ of the $\zeta_{\rm tail}$ to take into account the possible mas excess of the over-threshold averaged compaction function $\bar{\mathcal{C}} > 2/5$ that can contribute of increasing the PBH mass due to accretion. To do that, we have considered a new length-scale $r_{\rm tail,2}$ as the scale for which the averaged $\bar{\mathcal{C}}_{\rm tail}$ integrated from $r_{\rm tail}$ (the location of the peak of $\mathcal{C}_{\rm tail}$) up to $r_{\rm tail,2}$ gives $\bar{\mathcal{C}}_{\rm tail} = 2/5$. Our intuition is based on the fact that all the extra mass excess above the critical value $\bar{\mathcal{C}}_{\rm tail} = 2/5$ will contribute to the PBH mass. In particular we find $r_{\rm tail,2}$ solving

$$\frac{2}{5} = \frac{3}{\left[r_{\text{tail},2}^{3}e^{3\zeta_{\text{tail}}(r_{\text{tail},2})} - r_{\text{tail}}^{3}e^{3\zeta_{\text{tail}}(r_{\text{tail}})}\right]} \int_{r_{\text{tail}}}^{r_{\text{tail},2}} \mathcal{C}_{\text{tail}}(r)(1 + r\zeta_{\text{tail}}')e^{3\zeta_{\text{tail}}(r)}r^{2}dr. \tag{A.1}$$

The result is shown in Fig.18. The new mass function for the bubble channel is shifted to larger mass values. The contribution to the fraction of PBHs in the form of dark matter from the bubble channel is increased by a factor ~ 5 , which indicates that it doesn't substantially change the result from our previous realistic estimation using $r_{\rm tail}$ as a length-scale. Numerical simulations will be needed to test this hypothesis.

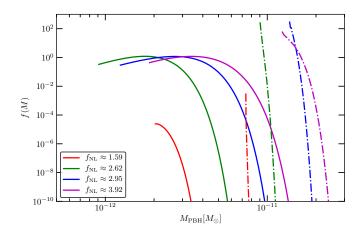


Figure 18. Mass function for the bubble channel, considering the length-scale of the fluctuation $\zeta_{\rm tail}$ as $r_{\rm tail}$ like in Fig.17 (solid line) and with $r_{\rm tail,2}$ (point-dashed line). The mass range of f(M) for the case $f_{\rm NL} \approx 2.95$ (blue line) and $f_{\rm NL} \approx 3.92$ (magenta line) have been shifted by a factor $\sim 2-4$ respectively for visualization purposes, like in Fig.17.

B Numerical parameters data

This appendix provides the numerical parameters that we have used to build the inflationary potential of Eq.(2.2) and proceed with the numerical simulations of bubble formation. In Table 1, we give the parameters for the cases fixing the critical threshold value for bubble formation $\nu_{b,c}$. In contrast, in Table 2, we provide the parameters that give cases for what the fraction of PBHs in the form of dark matter is $f_{\text{PBH}}^{\text{tot}} = 1 \pm 0.03$. All parameters have been chosen to fulfill the CMB requirements at the pivot scale and to have the power spectrum peak $\mathcal{P}_{\zeta_G}(k_{\text{max}})$, in a wave-mode scale k_{max} such that the corresponding horizon mass lies in the range $M_k(k_{\text{max}}) \in [10^{-13}, 10^{-12}] M_{\odot}$.

$A(\nu_{b,c} = 8 \pm 0.1)$	$\frac{\sigma^2}{10^{-4}}$	ϕ_0	$\frac{V_0}{10^{-3}}$	$f_{ m NL}$	$\frac{\mathcal{P}_{\zeta_G}(k_{\text{pivot}})}{10^{-9}}$	$\frac{n_s}{10^{-1}}$	$N_{\rm end} - N_{ m pivot}$
0.00234823544814031	4.2	3.925	3.53	0.69	2.09	9.59	54.19
0.00204353827240769	3	3.93	3.53	1.13	2.17	9.60	52.18
0.0018507625124141	2.25	3.925	3.54	1.59	2.24	9.60	51.28
0.00148802386561789	1.5	4	3.53	2.08	2.30	9.61	51.39
0.00134343266747832	1.29	4.048	3.505	2.21	2.28	9.61	51.70
0.00126306699654353	1.05	4.048	3.5	2.62	2.26	9.61	51.30
0.00120933210369861	0.9	4.048	3.5	2.95	2.26	9.61	51.06
0.00115206525841421	0.75	4.048	3.505	3.36	2.28	9.61	50.83
0.00111555573420713	0.66	4.048	3.5	3.68	2.26	9.61	50.69
0.00109008478843295	0.6	4.048	3.5	3.92	2.26	9.61	50.60
0.00106811486865607	0.55	4.048	3.495	4.15	2.25	9.61	50.52
0.00102153747766813	0.45	4.048	3.495	4.72	2.25	9.61	50.37
0.000983754231379358	0.375	4.048	3.495	5.28	2.25	9.61	50.26
0.000942745243336801	0.3	4.048	3.495	6.04	2.25	9.61	50.15

$A(\nu_{b,c} = 10 \pm 0.05)$	$A(\nu_{b,c} = 12 \pm 0.05)$
0.00234815594028443	0.00234808087098397
0.00204342623486182	0.00204331588405784
0.00185061586509428	0.00185046635285446
0.00148783955909958	0.00148766634984688
0.00134324912490089	0.00134307577203213
0.0012628683408432	0.00126266364856562
0.00120911430742841	0.00120887830114502
0.00115180495570062	0.00115153762505408
0.00111526841065318	0.00111498540297226
0.00108980550543697	0.00108950683584457
0.00106778894428082	0.00106749023768939
0.00102120421557745	0.0010208741850228
0.000983429190676518	0.00098309908693459
0.000942412857224492	0.000942113906988106

Table 1. Parameters for the case fixing the value $\nu_{b,c}=8\pm0.1$ (top table). The initial values chosen for solving the inflaton's homogeneous background dynamics are in the range $\phi_{\rm ini}\in[5.33-5.39]$. Parameter A for the case fixing the value $\nu_{b,c}=10\pm0.05$ and $\nu_{b,c}=12\pm0.05$ (bottom table). The corresponding values σ , ϕ_0 and V_0 are the same as in the top table. The other values $f_{\rm NL}$, $\frac{\mathcal{P}_{\zeta_G}(k_{\rm pivot})}{10^{-9}}$, $\frac{n_s}{10^{-1}}$ and $N_{\rm end}-N_{\rm pivot}$ for the cases $\nu_{b,c}\sim10,12$ are very similar to the case $\nu_{b,c}\sim8$ and are not shown.

A	$\frac{\sigma^2}{10^{-4}}$	ϕ_0	$\frac{V_0}{10^{-3}}$	$f_{ m NL}$	$\frac{\mathcal{P}_{\zeta_G}(k_{\text{pivot}})}{10^{-9}}$	$\frac{n_s}{10^{-1}}$	$N_{ m end} - N_{ m pivot}$
0.00185061	2.25	3.925	3.54	1.59	2.24	0.960	51.16
0.0012630165	1.05	4.048	3.5	2.62	2.26	0.961	51.28
0.001209285	0.9	4.048	3.5	2.95	2.26	0.961	51.04
0.001090017	0.6	4.048	3.5	3.92	2.26	0.961	50.58

	$\nu_{b,c}$	$ u_{\star}$	$\nu_{a,c}$	$\mathcal{P}_{\zeta_G}(k_{ ext{max}})$	$f_{ m PBH}^{ m tot(adiabatic)}$	$f_{ m PBH}^{ m tot(bubble)}$
	10.09	10.31	8.57	$2.28 \cdot 10^{-3}$	1.021	$3.33 \cdot 10^{-6}$
	8.55	8.95	8.55	$1.28 \cdot 10^{-3}$	$7.36 \cdot 10^{-2}$	0.928
Ī	8.51	9.08	8.85	$1.00 \cdot 10^{-3}$	$2.58 \cdot 10^{-3}$	1.025
	8.52	9.94	9.94	$4.95 \cdot 10^{-4}$	$3.57 \cdot 10^{-8}$	0.981

Table 2. Parameters for the case of fixing the total fraction of PBHs in the form of dark matter to be $f_{\rm PBH}^{\rm tot}=1\pm0.03$. The initial values chosen for solving the inflaton's homogeneous background dynamics are in the range $\phi_{\rm ini}\in[5.33-5.39]$.

It is important to notice that in Table 1 not all the digits for A are significant. For instance, a change $\delta A \sim 10^{-8}$ in the amplitude of the barrier of the potential will reduce the fraction $f_{\rm PBH}^{\rm tot}$ by 10^{-1} . But we show all the digits used in the simulations for clarity to the reader

References

- V. Atal, J. Cid, A. Escrivà and J. Garriga, PBH in single field inflation: the effect of shape dispersion and non-Gaussianities, J. Cosmology Astropart. Phys. 2020 (2020) 022 [1908.11357].
- [2] Y.B. Zel'dovich and I.D. Novikov, *The Hypothesis of Cores Retarded during Expansion and the Hot Cosmological Model*, Soviet Ast. **10** (1967) 602.
- [3] S. Hawking, Gravitationally collapsed objects of very low mass, Mon. Not. Roy. Astron. Soc. 152 (1971) 75.
- [4] B. Carr and S. Hawking, Black holes in the early Universe, MNRAS 168 (1974) 399.
- [5] B. Carr, The primordial black hole mass spectrum., ApJ 201 (1975) 1.
- [6] I.D. Novikov, A.G. Polnarev, A.A. Starobinskii and I.B. Zeldovich, *Primordial black holes*, A&A 80 (1979) 104.
- [7] A. Escrivà, F. Kuhnel and Y. Tada, Primordial Black Holes, 2211.05767.
- [8] G.F. Chapline, Cosmological effects of primordial black holes, Nature 253 (1975) 251.
- [9] B. Carr, F. Kühnel and M. Sandstad, Primordial black holes as dark matter, Phys. Rev. D 94 (2016) 083504 [1607.06077].
- [10] J. García-Bellido, Massive Primordial Black Holes as Dark Matter and their detection with Gravitational Waves, in Journal of Physics Conference Series, vol. 840 of Journal of Physics Conference Series, p. 012032, May, 2017, DOI [1702.08275].
- [11] B. Carr and F. Kühnel, Primordial Black Holes as Dark Matter: Recent Developments, Annual Review of Nuclear and Particle Science 70 (2020) 355 [2006.02838].
- [12] B. Carr, K. Kohri, Y. Sendouda and J. Yokoyama, Constraints on primordial black holes, Rept. Prog. Phys. 84 (2021) 116902 [2002.12778].
- [13] A.M. Green and B.J. Kavanagh, Primordial black holes as a dark matter candidate, Journal of Physics G Nuclear Physics 48 (2021) 043001 [2007.10722].
- [14] B. Carr and F. Kühnel, Primordial black holes as dark matter candidates, SciPost Phys. Lect. Notes 48 (2022) 1 [2110.02821].
- [15] M. Sasaki, T. Suyama, T. Tanaka and S. Yokoyama, Primordial black holes—perspectives in gravitational wave astronomy, Classical and Quantum Gravity 35 (2018) 063001 [1801.05235].
- [16] B. Abbott, others, LIGO Scientific Collaboration and Virgo Collaboration, Binary Black Hole Mergers in the First Advanced LIGO Observing Run, Physical Review X 6 (2016) 041015 [1606.04856].
- [17] R. Abbott, others, The LIGO Scientific Collaboration, the Virgo Collaboration and the KAGRA Collaboration, GWTC-3: Compact Binary Coalescences Observed by LIGO and Virgo During the Second Part of the Third Observing Run, arXiv e-prints (2021) arXiv:2111.03606 [2111.03606].
- [18] R. Murgia, G. Scelfo, M. Viel and A. Raccanelli, Lyman-α Forest Constraints on Primordial Black Holes as Dark Matter, Phys. Rev. Lett. 123 (2019) 071102 [1903.10509].
- [19] P. Ivanov, P. Naselsky and I. Novikov, Inflation and primordial black holes as dark matter, Phys. Rev. D 50 (1994) 7173.
- [20] J. Garriga and A. Vilenkin, Black holes from nucleating strings, Phys. Rev. D 47 (1993) 3265 [hep-ph/9208212].
- [21] H. Deng, J. Garriga and A. Vilenkin, *Primordial black hole and wormhole formation by domain walls*, *JCAP* **04** (2017) 050 [1612.03753].

- [22] J. Garriga, A. Vilenkin and J. Zhang, Black holes and the multiverse, JCAP 02 (2016) 064 [1512.01819].
- [23] J. Garriga and A. Vilenkin, Watchers of the multiverse, JCAP 05 (2013) 037 [1210.7540].
- [24] A. Kusenko, M. Sasaki, S. Sugiyama, M. Takada, V. Takhistov and E. Vitagliano, Exploring Primordial Black Holes from the Multiverse with Optical Telescopes, Phys. Rev. Lett. 125 (2020) 181304 [2001.09160].
- [25] J. He, H. Deng, Y.-S. Piao and J. Zhang, Implications of GWTC-3 on primordial black holes from vacuum bubbles, 2303.16810.
- [26] H. Deng, A. Vilenkin and M. Yamada, CMB spectral distortions from black holes formed by vacuum bubbles, JCAP 07 (2018) 059 [1804.10059].
- [27] V. Atal, J. Garriga and A. Marcos-Caballero, *Primordial black hole formation with non-Gaussian curvature perturbations*, *JCAP* **09** (2019) 073 [1905.13202].
- [28] H. Deng, Primordial black hole formation by vacuum bubbles. Part II, J. Cosmology Astropart. Phys. 2020 (2020) 023 [2006.11907].
- [29] S.S. Mishra and V. Sahni, Primordial Black Holes from a tiny bump/dip in the Inflaton potential, JCAP 04 (2020) 007 [1911.00057].
- [30] R. Zheng, S. Jiaming and T. Qiu, On primordial black holes and secondary gravitational waves generated from inflation with solo/multi-bumpy potential *, Chin. Phys. C 46 (2022) 045103 [2106.04303].
- [31] Q. Wang, Y.-C. Liu, B.-Y. Su and N. Li, Primordial black holes from the perturbations in the inflaton potential in peak theory, Phys. Rev. D 104 (2021) 083546 [2111.10028].
- [32] K. Rezazadeh, Z. Teimoori, S. Karimi and K. Karami, Non-Gaussianity and secondary gravitational waves from primordial black holes production in α-attractor inflation, Eur. Phys. J. C 82 (2022) 758 [2110.01482].
- [33] L. Iacconi, H. Assadullahi, M. Fasiello and D. Wands, Revisiting small-scale fluctuations in α -attractor models of inflation, JCAP **06** (2022) 007 [2112.05092].
- [34] A.A. Starobinsky, A New Type of Isotropic Cosmological Models Without Singularity, Phys. Lett. B 91 (1980) 99.
- [35] C. Germani and T. Prokopec, On primordial black holes from an inflection point, Phys. Dark Univ. 18 (2017) 6 [1706.04226].
- [36] V. Atal and C. Germani, The role of non-gaussianities in primordial black hole formation, Physics of the Dark Universe 24 (2019) 100275.
- [37] G. Ballesteros and M. Taoso, Primordial black hole dark matter from single field inflation, Phys. Rev. D 97 (2018) 023501 [1709.05565].
- [38] G. Ballesteros, J. Rey, M. Taoso and A. Urbano, Primordial black holes as dark matter and gravitational waves from single-field polynomial inflation, JCAP 07 (2020) 025 [2001.08220].
- [39] V.F. Mukhanov, H.A. Feldman and R.H. Brandenberger, Theory of cosmological perturbations. Part 1. Classical perturbations. Part 2. Quantum theory of perturbations. Part 3. Extensions, Phys. Rept. 215 (1992) 203.
- [40] J.M. Maldacena, Non-Gaussian features of primordial fluctuations in single field inflationary models, JHEP 05 (2003) 013 [astro-ph/0210603].
- [41] M. Sasaki, Gauge Invariant Scalar Perturbations in the New Inflationary Universe, Prog. Theor. Phys. 70 (1983) 394.
- [42] V.F. Mukhanov, The quantum theory of gauge-invariant cosmological perturbations, Zhurnal Eksperimentalnoi i Teoreticheskoi Fiziki 94 (1988) 1.

- [43] T.S. Bunch, P.C.W. Davies and R. Penrose, Quantum field theory in de sitter space: renormalization by point-splitting, Proceedings of the Royal Society of London. A. Mathematical and Physical Sciences 360 (1978) 117 [https://royalsocietypublishing.org/doi/pdf/10.1098/rspa.1978.0060].
- [44] V. Mukhanov, Physical Foundations of Cosmology, Cambridge University Press, Oxford (2005), 10.1017/CBO9780511790553.
- [45] G. Tasinato, An analytic approach to non-slow-roll inflation, Phys. Rev. D 103 (2021) 023535 [2012.02518].
- [46] Planck collaboration, Planck 2018 results. X. Constraints on inflation, Astron. Astrophys. 641 (2020) A10 [1807.06211].
- [47] Planck collaboration, Planck 2018 results. VI. Cosmological parameters, Astron. Astrophys. 641 (2020) A6 [1807.06209].
- [48] S. Dodelson and L. Hui, A Horizon ratio bound for inflationary fluctuations, Phys. Rev. Lett. 91 (2003) 131301 [astro-ph/0305113].
- [49] A.R. Liddle and S.M. Leach, How long before the end of inflation were observable perturbations produced?, Phys. Rev. D 68 (2003) 103503 [astro-ph/0305263].
- [50] J. Haro and L. Aresté Saló, Note on the reheating temperature in Starobinsky-type potentials, Gen. Rel. Grav. 52 (2020) 116 [2005.14653].
- [51] G. Domenech, J.-O. Gong and M. Sasaki, Consistency relation and inflaton field redefinition in the δN formalism, Phys. Lett. B 769 (2017) 413 [1606.03343].
- [52] S. Pi and M. Sasaki, Logarithmic Duality of the Curvature Perturbation, 2211.13932.
- [53] L. Verde and S. Matarrese, Detectability of the Effect of Inflationary Non-Gaussianity on Halo Bias, ApJ 706 (2009) L91 [0909.3224].
- [54] Y.-F. Cai, X. Chen, M.H. Namjoo, M. Sasaki, D.-G. Wang and Z. Wang, Revisiting non-Gaussianity from non-attractor inflation models, J. Cosmology Astropart. Phys. 2018 (2018) 012 [1712.09998].
- [55] Y.-F. Cai, X.-H. Ma, M. Sasaki, D.-G. Wang and Z. Zhou, Highly non-Gaussian tails and primordial black holes from single-field inflation, JCAP 12 (2022) 034 [2207.11910].
- [56] R. Kawaguchi, T. Fujita and M. Sasaki, *Highly asymmetric probability distribution from a finite-width upward step during inflation*, 2305.18140.
- [57] J.M. Bardeen, J.R. Bond, N. Kaiser and A.S. Szalay, The Statistics of Peaks of Gaussian Random Fields, ApJ 304 (1986) 15.
- [58] M. Shibata and M. Sasaki, Black hole formation in the Friedmann universe: Formulation and computation in numerical relativity, Phys. Rev. D 60 (1999) 084002 [gr-qc/9905064].
- [59] Y. Tanaka and M. Sasaki, Gradient expansion approach to nonlinear superhorizon perturbations. II. A Single scalar field, Prog. Theor. Phys. 118 (2007) 455 [0706.0678].
- [60] D.H. Lyth, K.A. Malik and M. Sasaki, A General proof of the conservation of the curvature perturbation, JCAP 05 (2005) 004 [astro-ph/0411220].
- [61] N.S. Sugiyama, E. Komatsu and T. Futamase, δN formalism, Phys. Rev. D 87 (2013) 023530 [1208.1073].
- [62] T. Harada, C.-M. Yoo, T. Nakama and Y. Koga, Cosmological long-wavelength solutions and primordial black hole formation, Phys. Rev. D 91 (2015) 084057.
- [63] A. Escrivà, C. Germani and R.K. Sheth, Universal threshold for primordial black hole formation, Phys. Rev. D 101 (2020) 044022.

- [64] A. Escrivà, C. Germani and R.K. Sheth, Analytical thresholds for black hole formation in general cosmological backgrounds, J. Cosmology Astropart. Phys. 2021 (2021) 030 [2007.05564].
- [65] M. Kopp, S. Hofmann and J. Weller, Separate Universes Do Not Constrain Primordial Black Hole Formation, Phys. Rev. D 83 (2011) 124025 [1012.4369].
- [66] A. Escrivà, PBH Formation from Spherically Symmetric Hydrodynamical Perturbations: A Review, Universe 8 (2022) 66 [2111.12693].
- [67] A. Escrivà, Simulation of primordial black hole formation using pseudo-spectral methods, Physics of the Dark Universe 27 (2020) 100466.
- [68] N. Kitajima, Y. Tada, S. Yokoyama and C.-M. Yoo, Primordial black holes in peak theory with a non-Gaussian tail, JCAP 10 (2021) 053 [2109.00791].
- [69] A. Escrivà, Y. Tada, S. Yokoyama and C.-M. Yoo, Simulation of primordial black holes with large negative non-Gaussianity, J. Cosmology Astropart. Phys. **2022** (2022) 012 [2202.01028].
- [70] J.C. Niemeyer and K. Jedamzik, Near-critical gravitational collapse and the initial mass function of primordial black holes, Phys. Rev. Lett. 80 (1998) 5481.
- [71] I. Hawke and J.M. Stewart, *The dynamics of primordial black-hole formation*, Classical and Quantum Gravity 19 (2002) 3687.
- [72] I. Musco and J.C. Miller, Primordial black hole formation in the early universe: critical behaviour and self-similarity, Classical and Quantum Gravity 30 (2013) 145009 [1201.2379].
- [73] Y. Tada and S. Yokoyama, Primordial black hole tower: Dark matter, earth-mass, and LIGO black holes, Phys. Rev. D 100 (2019) 023537 [1904.10298].
- [74] C.R. Evans and J.S. Coleman, Critical phenomena and self-similarity in the gravitational collapse of radiation fluid, Phys. Rev. Lett. 72 (1994) 1782 [gr-qc/9402041].
- [75] A. Escrivà and A.E. Romano, Effects of the shape of curvature peaks on the size of primordial black holes, JCAP 05 (2021) 066 [2103.03867].
- [76] G. Van Rossum and F.L. Drake, *Python 3 Reference Manual*, CreateSpace, Scotts Valley, CA (2009).
- [77] C.R. Harris, K.J. Millman, S.J. van der Walt, R. Gommers, P. Virtanen, D. Cournapeau et al., *Array programming with NumPy*, *Nature* **585** (2020) 357.
- [78] P. Virtanen, R. Gommers, T.E. Oliphant, M. Haberland, T. Reddy, D. Cournapeau et al., SciPy 1.0: Fundamental Algorithms for Scientific Computing in Python, Nature Methods 17 (2020) 261.
- [79] V. Atal, A. Sanglas and N. Triantafyllou, NANOGrav signal as mergers of Stupendously Large Primordial Black Holes, JCAP 06 (2021) 022 [2012.14721].
- [80] V. Atal and G. Domènech, Probing non-Gaussianities with the high frequency tail of induced gravitational waves, JCAP 06 (2021) 001 [2103.01056].
- [81] J. Kristiano and J. Yokoyama, Ruling Out Primordial Black Hole Formation From Single-Field Inflation, 2211.03395.
- [82] H. Motohashi and Y. Tada, Squeezed bispectrum and one-loop corrections in transient constant-roll inflation, JCAP 08 (2023) 069 [2303.16035].
- [83] J. Fumagalli, Absence of one-loop effects on large scales from small scales in non-slow-roll dynamics, 2305.19263.
- [84] Y. Tada, T. Terada and J. Tokuda, Cancellation of quantum corrections on the soft curvature perturbations, 2308.04732.

- [85] C. Gundlach and J.M. Martin-Garcia, Critical phenomena in gravitational collapse, Living Rev. Rel. 10 (2007) 5 [0711.4620].
- [86] C.L. Wainwright, M.C. Johnson, H.V. Peiris, A. Aguirre, L. Lehner and S.L. Liebling, Simulating the universe(s): from cosmic bubble collisions to cosmological observables with numerical relativity, JCAP 03 (2014) 030 [1312.1357].
- [87] M.J. Berger and J. Oliger, Adaptive Mesh Refinement for Hyperbolic Partial Differential Equations, Journal of Computational Physics 53 (1984) 484.
- [88] C.-M. Yoo, T. Harada, J. Garriga and K. Kohri, PBH abundance from random Gaussian curvature perturbations and a local density threshold, arXiv e-prints (2018) arXiv:1805.03946 [1805.03946].
- [89] H. Deng and A. Vilenkin, Primordial black hole formation by vacuum bubbles, JCAP 12 (2017) 044 [1710.02865].
- [90] B.J. Carr, K. Kohri, Y. Sendouda and J. Yokoyama, Constraints on primordial black holes from the Galactic gamma-ray background, Phys. Rev. D 94 (2016) 044029 [1604.05349].
- [91] B.J. Carr, K. Kohri, Y. Sendouda and J. Yokoyama, New cosmological constraints on primordial black holes, Phys. Rev. D 81 (2010) 104019 [0912.5297].
- [92] M. Boudaud and M. Cirelli, Voyager 1 e[±] Further Constrain Primordial Black Holes as Dark Matter, Phys. Rev. Lett. 122 (2019) 041104 [1807.03075].
- [93] S.K. Acharya and R. Khatri, CMB and BBN constraints on evaporating primordial black holes revisited, JCAP **06** (2020) 018 [2002.00898].
- [94] J. Chluba, A. Ravenni and S.K. Acharya, Thermalization of large energy release in the early Universe, Mon. Not. Roy. Astron. Soc. 498 (2020) 959 [2005.11325].
- [95] H. Niikura et al., Microlensing constraints on primordial black holes with Subaru/HSC Andromeda observations, Nature Astron. 3 (2019) 524 [1701.02151].
- [96] B. Carr, F. Kuhnel and L. Visinelli, Constraints on Stupendously Large Black Holes, Mon. Not. Roy. Astron. Soc. 501 (2021) 2029 [2008.08077].
- [97] H. Deng, μ -distortion around stupendously large primordial black holes, JCAP 11 (2021) 054 [2106.09817].
- [98] K. Kohri, T. Nakama and T. Suyama, Testing scenarios of primordial black holes being the seeds of supermassive black holes by ultracompact minihalos and CMB μ-distortions, Phys. Rev. D 90 (2014) 083514 [1405.5999].
- [99] T. Nakama, B. Carr and J. Silk, Limits on primordial black holes from μ distortions in cosmic microwave background, Phys. Rev. D 97 (2018) 043525 [1710.06945].
- [100] C. Ünal, E.D. Kovetz and S.P. Patil, Multimessenger probes of inflationary fluctuations and primordial black holes, Phys. Rev. D 103 (2021) 063519 [2008.11184].